Multiscale methods for simulation of paper making

Gustav Kettil

Department of Mathematical Sciences
Division of Mathematics
Chalmers University of Technology and University of Gothenburg
Gothenburg, Sweden 2019

Multiscale methods for simulation of paper making
Gustav Kettil

Abstract

In this work, multiscale methods for simulation of paper making are developed. The emphasis is on simulation of the paper forming process and simulation of the mechanical properties of paper sheets.

To simulate paper forming, a novel fiber-fiber interaction method is proposed. The method is developed to handle contact forces active on scales down to tens of nanometres. The DLVO theory, based on van der Waals and electrostatic forces, governs the fiber-fiber interaction together with a repulsion force developed to assure numerical stability for fiber motion resolved with discrete time stepping. The interaction method is incorporated as one of four sub-models in a fiber suspension model. The other three sub-models are a fluid model governed by Navier-Stokes equations, a fiber model governed by beam theory, and a fluid-fiber and fiber-fluid interaction model based on an immersed boundary method and experimental drag force expressions. The fiber suspension model is used to simulate fiber lay downs onto an industrial forming fabric. The resulting virtual fiber sheets are investigated by simulation of the air flow through the sheets. The simulated permeabilities agree well with experimental data for sheets with low density. The proposed framework is able to create three-dimensional fiber networks which can be used for investigation of mechanical or penetration properties of the sheets.

The flow conditions during the initial state of paper forming is studied by simulating the flow over cylinder configurations and three industrial forming fabrics. The impact from the structures on the upstream flow is analysed. Novel impact measures are defined to improve the characterization of forming fabrics and their impact on the flow.

For simulation of the mechanical properties of paper sheets, a numerical multiscale method for discrete network models is developed. A fiber network model is proposed, representing fibers and bonds as edges and nodes. In the numerical multiscale method, the fiber network is approximated by a coarse grid, which together with bilinear basis functions defines a low-dimensional coarse space. The coarse space is modified by solving sub-local problems resulting in corrections of the bilinear basis functions. The resulting corrected basis spans a low-dimensional multiscale space with good approximation properties for unstructured heterogeneous networks with highly varying properties. Numerical examples show that the proposed method has optimal order convergence rates for such complex networks.

Keywords: Paper making, Fiber suspension flow, Virtual paper sheets, Multiscale methods, Fiber-fiber interaction, Lay down simulations, Fluid structure interaction, Forming fabric flow, Numerical upscaling, Fiber network model

List of Papers

- **Paper I**. G. Kettil, A. Mark, F. Svelander, R. Lai, L. Martinsson, K. Wester, M. Fredlund, M. Rentzhog, U. Nyman, J. Tryding, and F. Edelvik, *Novel contact forces for immersed boundary paper forming simulations*, conference proceeding TAPPI, Atlanta, USA, April 2015.

- **Paper II**. G. Kettil, A. Mark, F. Svelander, R. Lai, K. Wester, M. Fredlund, M. Rentzhog, and F. Edelvik, *Detailed simulations of early paper forming*, conference proceeding COST Action FP1005, Trondheim, Norway, June 2015.

- **Paper III**. G. Kettil, A. Målqivst, A. Mark, F. Edelvik, M. Fredlund, and K. Wester, *A multiscale methodology for simulation of mechanical properties of paper*, conference proceeding 6th European Conference on Computational Mechanics, Glasgow, UK, June 2018.

- **Paper IV**. G. Kettil, A. Mark, K. Wester, M. Fredlund, and F. Edelvik, *Numerical investigation of upstream cylinder flow and characterization of forming fabrics*, submitted.

- **Paper V**. G. Kettil, A. Målqvist, A. Mark, M. Fredlund, K. Wester, and F. Edelvik, *Numerical upscaling of discrete network models*, submitted.

- **Paper VI**. G. Kettil, A. Mark, A. Målqivst, F. Svelander, K. Wester, M. Fredlund, and F. Edelvik, *Simulation of paper forming using immersed boundary techniques and a novel fiber interaction method*, submitted.

Contributions of the Author

- **Paper I**. Kettil developed and implemented the interaction model, performed the lay down simulations, and wrote the manuscript.

- **Paper II**. Kettil extended the simulation framework with a pressing approach, extended the interaction model to rectangular cross sections, implemented the new extensions, performed the simulations, and wrote the manuscript.

- **Paper III**. Kettil proposed and presented the methodology for a multiscale simulation framework, developed and implemented the network model, and wrote the manuscript.

- **Paper IV**. Kettil performed the simulations, defined the impact measures, analysed the results, and wrote the manuscript.

- **Paper V**. Kettil had a major role in the development of the numerical upscaling method, implemented the method, analysed the method theoretically, contributed to the error analysis of the method, developed and implemented the network model, performed the numerical experiments, and wrote the main part of the manuscript.

- **Paper VI**. Kettil extended the interaction model to its given version, improved the simulation framework, developed and implemented the periodic boundary condition for object interaction, performed the simulations, and wrote the manuscript.

Acknowledgments

To Allis, Bertil, Bertil and Ingeborg

Contents

Nomenclature

Flow over forming fabrics and cylinders

μ	Dynamic viscosity of fluid	Ns/m^2
ρ	Fluid density	kg/m^3
A_a^Γ	Area-measure	1
d	Cylinder/thread diameter	m
D^Γ	Variation-measure	1
D_a^Γ	Length related variation-measure	1
g	Normalized horizontal surface spacing	1
I_a^Γ	Velocity field indicator function	1
l	Normalized vertical surface spacing	1
L_a^Γ	Length-measure	1
L_B	Distance from cylinder to boundary parallel to main stream velocity	m
L_I	Distance from inlet to closest cylinder	m
L_O	Distance from outlet to closest cylinder	m
M_Γ	Maximum value function	1
m_Γ	Minimum value function	1
Re	Reynolds number based on cylinder/thread diameter	1
S	Surface spacing	m
S_x	Horizontal surface spacing	m
S_y	Vertical surface spacing	m
V_0	Mainstream velocity	m/s

Multiscale method for network models

$\bar{h}_i$	Average length of edges connected to degree of freedom i	m
$\mathcal{M}$	Set of indices of active degrees of freedom of coarse nodes	
ϕ_i	Correction vector for basis vector i	1
π_H	Bilinear weighted interpolant	
ρ	Patch size parameter	1

$\tilde{u}_{\mathrm{ms}}$	Multiscale solution vector of localized problem	m
$\tilde{V}_{\mathrm{ms}}$	Localized multiscale space	
$\|\|\cdot\|\|$	Energy norm	
B_H	Basis vector matrix (prolongation matrix)	1
C_H	Restriction matrix	1
d	Dimension of the space the network resides in	
F	Load vector	N
H	Size of the coarse grid elements	m
K	Connectivity matrix	N/m
m	Total number of degrees of freedom of coarse nodes	1
m_H	Number of active degrees of freedom of coarse nodes	1
n	Total number of degrees of freedom of network nodes	1
u	Solution vector	m
u_{ms}	Multiscale solution vector	m
V	Solution space	
V_{ms}	Multiscale space	
V_H	Coarse space	
W	Detail space	
$\bar{F}$	Scaled load vector	N/m^2
$\check{F}$	Load vector with constrained degrees of freedom	N
$\check{K}$	Connectivity matrix with constrained degrees of freedom	N/m
Λ_i	Bilinear basis function of coarse node i	1
λ_i	Interpolation of bilinear basis function Λ_i	1

Fiber network model

(i,j)	Edge connecting nodes i and j	
(i,j,l)	Edge pair connecting nodes i, j and l	
ΔL_{ij}	Length change of edge (i,j)	m
$\Delta\theta_{ijl}$	Total angle change of edge pair (i,j,l)	rad
$\delta\theta_{ji}$	Angle change of edge (i,j)	rad
δ_i	Displacement of node i	m
η_{ijl}	Stiffness parameter of edge pair (i,j,l)	Pa
γ_{ijl}	Poisson parameter of edge pair (i,j,l)	1
$\hat{z}$	Out-of-plane normal	1
κ_{ijl}	Angular resistance parameter of edge pair (i,j,l)	Pa
$\mathcal{E}$	Set of edges	
$\mathcal{N}$	Set of node indices	
$\mathcal{P}$	Set of edge pairs	
d_{ij}^a	Direction vector of edge (i,j) with respect to node a	1
F	Node load vector	N
$F_a^{\mathrm{I}}(i,j), F_a^{\mathrm{II}}(i,j,l), F_a^{\mathrm{III}}(i,j,l)$ The three force contributions		N
K	Elasticity/connectivity matrix	N/m
k_{ij}	Stiffness parameter of edge (i,j)	Pa

$K_{ij}^{\mathrm{I}}, K_{ijl}^{\mathrm{II}}, K_{ijl}^{\mathrm{III}}$	Element matrices	N/m
L_{ij}	Length of edge (i,j)	m
N	Total number of nodes	1
n_{ji}^j, n_{jl}^j	Edge normals of edge pair (i,j,l)	1
p_i	Position of node i	m
u	Node displacement vector	m
V_{ijl}	Joint volume parameter of edge pair (i,j,l)	m^3
w_{ij}	Width of edge (i,j)	m
z	Out-of-plane thickness of edges	m

Suspension model and paper forming simulation framework

$\bar{d}$	Mean diameter of fiber cross section	m
$\bar{F}_i$	Averaged force for contact point i	N
$\bar{Y}_1^0, \bar{Y}_2^0$	Effective surface potentials of two interacting contact points	1
Δp	Pressure drop	Pa
Δt	Fiber time step	s
$\hat{n}$	Direction vector pointing between two contact points	1
κ	Inverse of the Debye length	1/m
μ	Dynamic viscosity of fluid	$\mathrm{Ns/m}^2$
$\psi_{d,i}$	Diffuse double layer potential of contact point i	V
ρ	Fluid density	$\mathrm{kg/m}^3$
σ_i^0	Surface charge of contact point i	$\mathrm{C/m}^2$
$\tilde{v}_{\mathrm{rel}}$	Relative velocity between contact points	m/s
ε	Liquid permittivity	F/m
$a_i(t)$	Acceleration of contact point i	$\mathrm{m/s}^2$
A_{12}	Hamaker constant	J
$a_{i,0}$	Intrinsic acceleration of the fiber corresponding to contact point i	$\mathrm{m/s}^2$
$B_i(h)$	Bell functions	1
C_D	Drag coefficient	1
D	Fiber diameter	m
e	Elementary charge	C
f_D	Drag force per unit length	N/m
F_E	Electrostatic force	N
F_i	Total force acting on contact point i	N
F_i^{D}	Drag force acting on contact point i	N
F_i^{G}	Gravitational force acting on contact point i	N
F_S	Steric repulsion force	N
F_W	van der Waals force	N
$F_{i,j}^{\mathrm{I}}$	Total contact force acting on point i from interaction with point j	N
$F_{S,i}$	Components of the steric repulsion force	N
$g_E(h)$	Short range extension of the electrostatic force	N
$g_W(h)$	Short range extension of the van der Waals force	N
h	Surface separation distance between two contact points	m

h_0	Minimum DLVO distance constant	m
$h_{\min}$	Minimal possible separation distance between two contact points	m
h_R	Parameter of the steric repulsion force	m
h_S	Parameter of the steric repulsion force	m
k	Boltzmann constant	J/K
L	Fiber length	m
M	Number of contact points	1
m_i	Mass of contact point i	kg
N	Number of fibers	1
p	Fluid pressure	Pa
$p_i(t)$	Position of contact point i	m
R	Distance between contact points	m
r_1, r_2	Representative radii of two interacting contact points	m
Re	Reynolds number of flow over fiber	1
T	Temperature	K
t	Time	s
t_R	Parameter of the steric repulsion force	s
u	Fluid velocity	m/s
v^{rel}	Relative velocity between fiber and fluid	m/s
$v_i(t)$	Velocity of contact point i	m/s
V_W	The van der Waals potential	Nm
$y_i(t)$	Auxiliary variable for equation system for contact points	

1. Introduction

Paper making is an over thousand years old craftsmanship. For the majority of this time, various hand making methods have been used. During the 19th century, the paper making process was industrialized and today paper machines all over the world produce immense amounts of paper. In 2013, the production amounted to 403 million tons of paper and cardboard [56]. Worldwide, on average about 60 kilograms of paper is used per person annually [2]. The main categories of products are publication paper, packaging paper and tissue paper.

The environmental impact of the paper industry is major in terms of energy consumption, chemical utilization and water usage. However, the base component in paper materials, the fiber, is a renewable resource. Therefore, the paper industry has a great potential to contribute to sustainability, and when developing countries are increasing their demand of classic paper products at the same time as the developed world searches for new ways to use paper, the paper industry will play an important role. Not only in terms of improving the sustainability of the process as such, but also in terms of developing new paper based materials.

The process of paper making is complex, and to improve paper products, increase the efficiency of the process, and develop new materials, innovative and advanced investigation methods are required. Experimental methods are one important approach, but due to the complexity of the process, many aspects of interest are difficult to measure and evaluate with experiments alone. Therefore, a necessary aid is the growing method of computer simulations, an approach which is based on mathematical modelling and high performance computing.

Paper consists of fibers and additional particles bonded together in a network structure. The configuration of this fiber network, together with the prop-

erties of the individual fibers and the bonds between them, are directly govern-
ing the main properties of paper. In the forming section of a paper machine, a
fiber suspension flows down onto a woven fabric. When the suspension reaches
the fabric, the fibers lay down and the paper sheet is formed.

Three important topics mentioned above - the properties of paper, the struc-
ture of paper, and the forming of the paper sheet - give rise to two important
questions. Firstly, how do the conditions during the forming process, such as
the fabric geometry or the flow features, affect the resulting structure of the
paper sheet? Secondly, how are properties such as stiffness and strength, or
permeability and penetration, depending on the structure of the paper? The
goal of this work is not to directly give answers to these questions, but to study
and develop methods which can be used to investigate these questions in detail
through simulation.

To facilitate studies of the questions in the previous paragraph, this work
aims to develop efficient methods for simulation of the forming process, and
for simulation of the mechanical properties of paper. The forming simulations
should be able to investigate the flow conditions during forming, the effect of
the forming fabric, and create realistic paper structures that can be used in the
second simulation tool. The framework for simulation of mechanical proper-
ties should ultimately be able to study important characteristics such as tensile
strength, tensile stiffness, bending stiffness, out-of-plane strength and fracture
propagation of macroscale paper samples.

One great challenge when modelling paper and its production process is
the multiscale features of paper. Paper is a heterogeneous macroscale material
whose properties are depending on the microscale structure of fibers bonded to-
gether. Moreover, paper is produced in huge machines, several orders of magni-
tude larger than single fibers. To simulate paper forming and paper properties,
methods are needed that can surmount the multiscale challenge, otherwise the
computational cost will be too large.

In this work, a paper forming simulation framework is presented. The
framework is based on a fiber suspension model with a novel fiber-fiber inter-
action method which includes the physical interaction forces present in paper
forming. Lay down simulations are performed and the resulting virtual sheets
are investigated by simulation of the air flow. The fundamentals of the upstream
flow during the initial sheet formation are studied by simulation of the flow over
cylinder configurations and industrial forming fabrics. Moreover, a numerical
upscaling method for discrete fiber networks is proposed, enabling large scale
simulation of mechanical properties of paper while still including single fibers
and bonds.

1.1 Background

The main constituent of paper is fibers, often wood fibers, but non-wood fibers such as cotton is also used. See Figure 1.1 for a microscope image of a paper sheet, visualising single wood fibers bonded together. During the logging process, timber is felled and transported to sawmills where the wood is chipped into small parts called wood chips. In a pulp mill, the wood chips are separated into individual fibers. This process is called pulping and the resulting mass of free fibers is called pulp. The fiber separation is achieved by mechanical or chemical means, or by a combination of the two, depending on the desired fiber properties. Next, the pulp is delivered to a paper mill. In an integrated mill, both the pulp and paper mill are located at the same site.
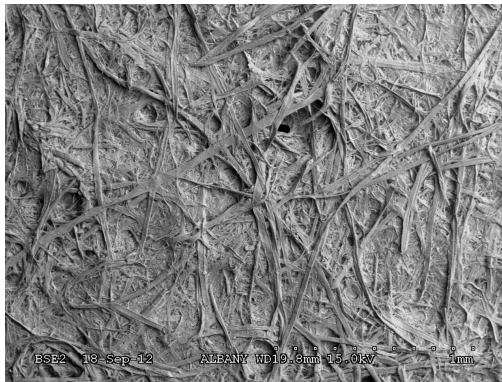
Figure 1.1: Scanning electron microscope (SEM) image of a paper sheet. The real size of the image is approximately 2.6×1.9 mm^2. Picture courtesy of Albany International.

Before the paper is created in a paper machine, the pulp is prepared to various degrees depending on the type of paper produced. During the bleaching process, the brightness of the pulp is increased. The most important preparation is the refining process, during which the pulp is treated mechanically to increase the surface area and conformability of the fibers, leading to improved bonding. Lastly, before entering the paper machine, in the stock preparation, the pulp is mixed with water and additives. A dilute suspension is important to enable the creation of a uniform paper sheet. Additives are added to improve the end product or to aid during the process. The resulting mixture, called stock, is then ready to enter the paper machine.

In the first part of the paper machine (see Figure 1.2 for a schematic overview

of a paper machine), the fiber suspension is contained in the headbox. The head-
box is a device that by pressure injects the suspension uniformly down onto the
wire, an endless woven fabric which runs at high speed and on which the fiber
web is built up, see Figure 1.3 for a snapshot of a wire. The aim of this part
of the machine, called the wet-end or the forming section, is to build up the
fiber web and to remove a large content of water through the holes of the wire.
In a classic fourdrinier machine, one wire is used. For twin wire formers, the
suspension is injected such that the web goes in between two wires and the
dewatering takes places on both sides. The wire is often called forming fabric.
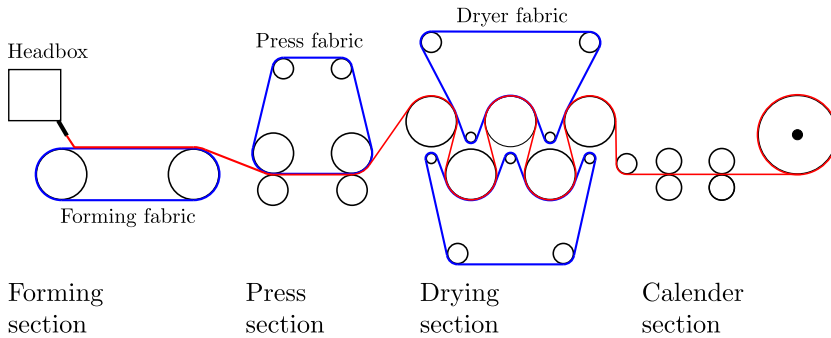
Figure 1.2: A schematic overview of a paper machine.

After the forming section, the paper moves on to the pressing section, where
large rolls compress the sheet to further remove water and smooth the paper
surface. Next, the fiber web goes into the largest and most energy consuming
part of the paper machine, the dryer section. With dryer felts and circulation
of heat through air, most of the remaining water content is removed. Lastly, in
the calender section, the paper is finished off by passing trough rolls to improve
surface properties such as smoothness and gloss.

In this work, methods for investigation of paper through simulation are de-
veloped and studied. The process described above is comprehensive, and the
scope of this work covers two main topics. First, simulation of the forming sec-
tion where the basic paper structure is built up, together with a simple approach
for simulation of pressing. Second, the resulting paper structure and how to
simulate its mechanical properties are considered.

To simulate paper forming, a mathematical model has to be developed which
describes how the fiber suspension flows down onto the forming fabric. Such a
model has to capture the dynamics of single fibers, the complex fluid flow over
the fabric, the interaction between fibers and fluid, and the interaction between

Figure 1.3: Triangulation of a small piece of a double layer forming fabric. The planar dimension of the fabric is 6.9×3.7 mm^2 and the height is 0.6 mm. The top side is where the fibers lay down.

fibers and between fibers and fabric.

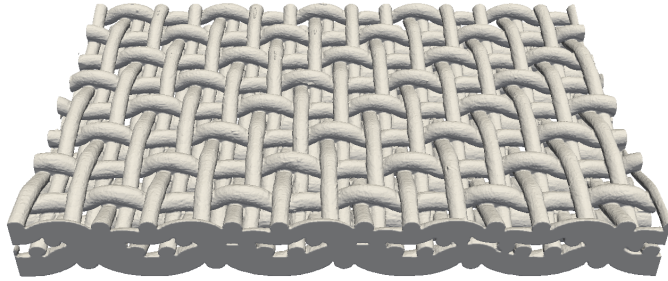Motion of single and multiple fibers in fluids has been studied since the beginning of the twentieth century [15, 16, 34], while simulations of particle motion in fluids were first accomplished in the middle of the 1980s [5]. In these first simulations, the particles were spheres and the fluid motion fixed, such as shear flow. During the following years, the models were extended to increasing complexity. The first fiber-like objects were studied in the beginning of the 1990s, by composing chains of spheres [68]. Later on, elements such as prolate spheroids [53] and also cylinders [55, 63, 64] were used to build up the fibers. Simultaneously, the complexity of the fluid was increased and in the end of the 1990s, flow governed by the Navier-Stokes equations was studied [61]. Different types of contact models were utilized during the progress. In this work, the fibers are modelled as beams, and the Navier-Stokes equations are solved using an immersed boundary method, enabling the flow over real industrial forming fabrics to be studied. Moreover, a novel method for calculating the chemical and physical interaction between fibers is developed, based on DLVO contact forces, known to be present between fibers [27]. DLVO is a theory of interaction between colloidal particles, based on van der Waals and electrostatic forces, named after Derjaguin, Landau, Verwey and Overbeek [10, 65].

The proposed fiber suspension model is the basis of the simulation framework presented in this work. The model and the framework are presented in Paper I, Paper II and Paper VI. The framework is used to simulate a simplification of the paper forming process, with thousands of fibers flowing down onto an industrial fabric. The resulting virtual paper sheets are studied by simulation of the air flow through the sheets.

Moreover, in Paper IV, the framework is used to study the fundamentals of upstream flow over forming fabrics. An increased understanding of this topic is desirable since the flow condition in the forming section governs the build up of the paper structure, which in the end defines the mechanical properties of paper. The study is initiated by first investigating flow over different configurations of cylinders, representing a two-dimensional simplification of fabrics. Flow over one and two cylinders has been studied extensively earlier, with emphasis on the downstream wake behaviour and mainly for large Reynolds numbers [71, 72]. However, the upstream features of flow over cylinders have not been investigated to any larger extent. The Reynolds regime in the forming section is 10-80 [18]. For flow over one cylinder, the transition from steady to unsteady flow occurs around $Re = 40$. This leads to a drastic change of the downstream flow behaviour. In this work, the upstream flow over different cylinders is investigated in the Reynolds number range 10-80. The studied configurations are one cylinder, two cylinders, and one and two rows of cylinders. To compare the flow properties for the different configurations, measures are proposed which characterize the impact from the structure on the upstream flow.

Experimental characterization of fabrics and their flow properties is an admittedly difficult task, due to the laborious nature of experimental measurements during paper making [36]. One common measure for characterization of fabrics is the CFM-value, quantifying the air flow per area through the fabric at a pressure drop of 125 Pa. However, this value alone does not give a proper flow characterization of fabrics. In this work, the flow over fabrics is simulated, and the measures proposed during the cylinder study are applied to the fabrics. Three different industrial forming fabrics are investigated and their properties are characterized. Moreover, also the drainage marking of the fabrics are investigated by analysing the periodicity of the upstream flow field.

In the second main topic of this work, the mechanical properties of paper is considered. To simulate mechanical properties of paper, one popular approach is to model the paper as a fiber network (see Figure 1.4), including each single fiber and the bonds in-between. There exists several such models with various complexity. Common for all these models are that they are built up of single elements representing the fibers, and that the elements are connected in some way. The network structure is in some works modelled as a regular lattice [67], but more commonly the network has an unstructured configuration as in real paper. The fibers are in the simplest cases modelled as rigid straight rods, and in more complex models, beams are used. No matter which model that is employed, investigation of fiber networks at a large scale and in three dimensions leads to numerical problems of huge size with high computational cost. To over-

come this difficulty, multiscale methods can be utilized. However, few methods have been developed for discrete networks. In this work, a numerical multiscale method for fiber networks is developed.
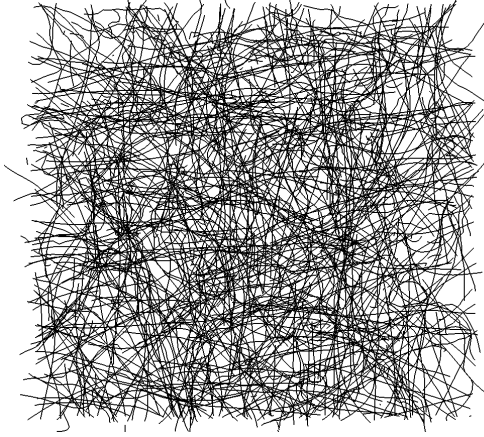
Figure 1.4: A fiber network representation of a small piece of a virtual paper sheet. The size of the network is 3×3 mm^2.

As a starting point for simulation of the mechanical properties of the virtual sheets attained from the forming simulations, and as a basis for the development of the multiscale method, a basic fiber network model is developed in this work. The network is modelled as consisting of edges and nodes. The fibers are represented as chains of edges and the fibers are connected to each other with mutual nodes or bonding edges. The governing equations for the network is attained by force equilibrium equations at each node. Three types of forces act at the nodes when they are displaced. First, a classic spring force resisting changes in length of the edges. Second, an angular spring force resisting changes in angles between connected edges. Third, a force acting to resist changes in the total length of pairs of edges, giving an effect similar to the Poisson effect.

Multiscale methods, also referred to as upscaling techniques, are much more common for partial differential equations (PDE) than for discrete network problems. Methods for numerical solution of PDE:s are often based on the idea of homogenization. Two examples are the Heterogeneous multiscale method [66], and the Multiscale finite element method [29]. A more recent method with relevance to this work, is the Localized orthogonal decomposition method (LOD) [46], which is inspired by the Variational multiscale method [28]. In regard of network models, multiscale methods have been de-

veloped for solving problems of material conductivity [14, 31], flow in porous medium [8], and traffic flows [9]. A few works on multiscale methods for fiber networks also exist, such as [3]. In this work, the LOD method is extended and modified for solving discrete fiber networks. The resulting numerical upscaling method is applicable to unstructured networks with varying fiber and bond properties, enabling investigation of the mechanical properties of macroscale paper sheets while still including the effects of single fibers and bonds. The proposed multiscale method gives optimal order convergence rate for unstructured and random networks. The network model and the numerical multiscale method are presented in Paper III and Paper V.

History of the research project

This work is part of the research and development project ISOP (Innovative Simulation of Paper) which is carried out at Fraunhofer-Chalmers Research Centre (FCC)[1] in collaboration with companies from the Swedish paper industry. The main purpose of the ISOP project is to predict macroscopic paper properties with industrially relevant accuracy through microstructure simulations. To accomplish this, mathematical models are being developed and implemented in IBOFlow[2] (Immersed Boundary Octree Flow Solver), an incompressible finite-volume based fluid solver developed at FCC.

The ISOP project started in January 2009, and the fourth three-year phase started in 2018. The project has three main modelling tracks: paper forming, edge wicking, and paper network modelling. These three tracks have been supported by several experimental campaigns. Single ply and two ply paper sheets were manufactured in a controlled environment at Packaging Greenhouse, and the paper pulp, retention, sizing and fillers were varied. Several experiments were performed to support the modelling tracks. From the experiments, air permeabilities, pressurized edge wick, contact angles, tensile strength, tensile stiffness, bending resistance, z-strength, and pore size distribution were extracted.

In the paper forming track, the model presented in this work has been developed. The aim of the model is to simulate the forming section of a paper machine and to use the resulting virtual paper board model as an input to the other tracks. The model was first published by Mark and co-workers in 2011 and 2012 [41, 62]. In these works, the fibers were modelled as beams, and the immersed boundary method [44] was used to handle the interaction between fluid and fibers. In this thesis, the paper forming model has been extended and refined to handle physical fiber contact forces. Further, a more advanced fiber

---

[1]http://www.fcc.chalmers.se/
[2]http://www.fcc.chalmers.se/software/ips/iboflow/

model [59] is included.

The simulated paperboard model or tomography is used as input for the edge wicking simulations. In edge wicking, the fluid penetration into the open edge of the paperboard is modelled. To calculate this, a multiscale framework has been developed. On the fiber microscale, a pore morphology method is used to calculate capillary pressure curves, and one-phase flow simulations performed in the active pores to calculate the relative permeabilities. The result is a database of capillary pressure curves and relative permeabilities as a function of saturation and porosity. The database is used as input for a two-phase flow simulation on a 2D virtual macro sheet to calculate the penetration of fluid in the paper. For details, see the resulting publications from 2012 and 2015 [35, 42, 43].

The newest part of the project was started in 2017, and is the development of a fiber network model and a multiscale method which will be used to investigate mechanical properties of paper, and especially the virtual paper sheets attained from the paper forming simulations.

The developed models have been integrated on the Industrial Path Solutions (IPS) software platform[3], and the modules IPS Edge Wicking and IPS Paper Forming have been delivered to the ISOP partners.

1.2   Outline of thesis

The outcome of this thesis work is divided into five topics which are described in one chapter each. The five topics are the following:

- Fiber suspension model (with the fiber-fiber interaction model).

- Paper forming simulation framework.

- Fabric flow investigation.

- Fiber network model.

- Multiscale method for discrete network models.

Each of these five chapters starts with a short motivation. For some topics, a review of earlier works in the corresponding field is included. Thereafter an overview of the theory and methods is given, summarizing the more detailed presentations in the papers. Selected results are presented where appropriate. Some additional contents not included in the papers are also added.

---

[3]http://industrialpathsolutions.se/

Following the five chapters of main contributions, a chapter with discussion and future work is given. After that chapter, short summaries of the six included papers are given, and lastly the six papers are included in their full length.

2. Fiber Suspension Model

The basic structure of paper is created during the lay down process in the forming section of the paper machine. Since the structure of the fiber sheet governs the properties of the paper product, it is important to study this process in detail. However, the complexity is significant due to the apparent scale differences and multi-physic features. The width of a paper machine can be ten meters. Fibers have a length of up to some millimeters and a width of around twenty micrometers. Moreover, the interaction forces present in a fluid suspension, for example electrostatic and van der Waals forces, act on distances of tens of nanometers.

In this work, a *fiber suspension model* is presented which takes into account each single fiber, the complex fluid flow, the interaction between fibers and fluid, and the interaction between the fibers and also the forming fabric. To make such a detailed model computationally applicable, a novel method for the calculation of the fiber-fiber and fiber-fabric interaction has been developed.

For a general suspension flow, that is, a fluid flow containing immersed objects, a general model can be assumed to consist of the following four submodels:

- Fluid model.
- Object model.
- Fluid-object and object-fluid interaction model.
- Object-object interaction model.

In this work, such a model is proposed and it is used to simulate the lay down process in the paper machine. In Figure 2.1, an illustration of the fiber suspension model during a lay down simulation is shown.
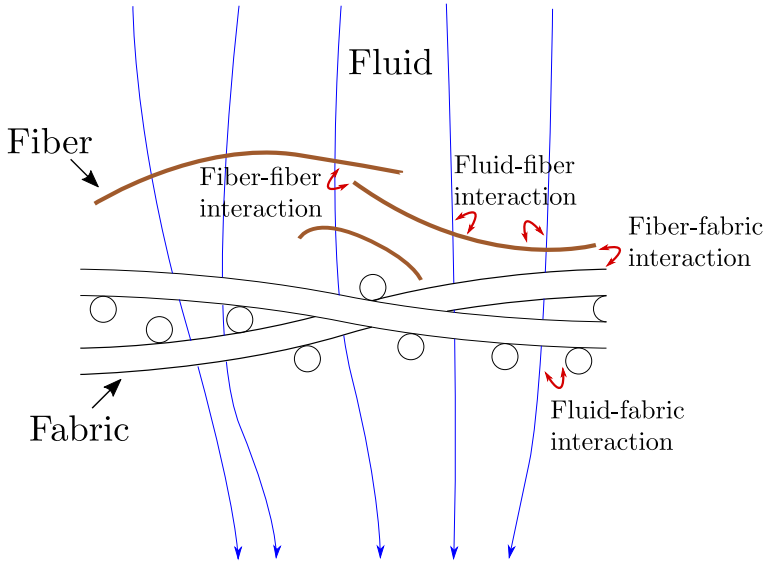
Figure 2.1: An illustration of the fiber suspension model and its sub-models for the case of a fiber lay down onto a forming fabric.

The fluid model predicts the behaviour of the fluid, and is in this work governed by the incompressible Navier-Stokes equations. The object model describes the immersed objects, and the choice can vary, depending on the type of included objects. Here fibers, modelled as beams, and a static rigid fabric are considered. The interaction between the fluid and objects is handled by an immersed boundary method for the object's effect on the fluid, and an empirical drag force relation for the fluid's effect on the fibers. The model for the interaction between objects is based on the DLVO forces. This novel interaction model makes it possible to resolve contact forces varying considerably over nanoscale, without requiring the fiber time step to be reduced, and is one of the main contributions of this work.

In Section 2.1, a summary of earlier works of simulation of suspension flows is presented. In the following four sections, the four sub-models are described. Lastly, the fiber-fiber interaction model is investigated by simulation of collision of two fibers.

2.1 Simulation methods for suspension flows

In this section, a review of simulation methods for suspension flows, with emphasize on fiber suspension flows, is presented. Before the simulation methods are presented, two paragraphs about theoretical and experimental works are given.

In 1922, Jeffery published a work [34] where he theoretically derived the motion of a single prolate spheroid in shear flow. The resulting equations show that the orbit of a prolate spheroid is periodic with no tendency to set its axes aligned in any particular direction. Jeffery's equations are often referred to, and compared with, when fiber motion in shear flow is investigated.

During the 1950s and 1960s, Mason and co-workers [15, 16] performed experiments with important results. They investigated fiber motion in shear flow and found results in accordance to Jeffery's equations, but also extending to flexible particles. The resultant fiber configurations are frequently used for comparison when developing simulation methods for fibers.

An early work on simulation of suspension flows was performed by Bossis and Brady in the mid 1980s [5, 6]. Their method, called Stokesian dynamics, was used to simulate a suspension of spherical particles in a shear flow at low Reynolds numbers. They considered solid rigid particles in a Newtonian fluid, whose motion was governed by Newton's second law. Two types of forces were considered to act on the particles, hydrodynamic forces and contact forces. By assuming a low Reynolds number, a large Péclet number, and absence of Brownian motion, the inertia could be neglected, reducing the complexity of the governing equations. For the hydrodynamic force, Bossis and Brady used theory derived by Brenner and co-workers [7, 22], applied to linear shear flow. The particle velocities were resolved and the new particle positions attained by time stepping, using a Runge-Kutta scheme. The model was used to simulate a monolayer of spherical particles. The interaction between particles was calculated from a repulsive force expression with a singularity at zero separation.

In the beginning of the 1990s, Yamamota and Matsuoaka developed a model for simulation of fibers [68–70]. In their approach, a fiber was modelled as built up of spheres with fixed radius. The spheres were bonded pairwise with three types of connections, including stretching, bending, and torsion, respectively. The three kinds of connections were governed by spring relations. The fiber motion was governed by the Newton-Euler equations. Linear shear flow was assumed and the governing equations were solved using a finite difference technique. A single fiber in shear flow was simulated and the resulting fiber

configurations were compared with the experimental results of Mason and co-workers [15,16]. In addition to simulations of a single fiber, multiple fibers were investigated. In the multi-body study, lubrication forces were used between the spheres, and a repulsive force was employed for the shortest separations to ensure numerical stability.

In 1997, Ross and Klingenberg [53] published a work with an approach similar to that of Yamamoto and Matsuoka, but instead of spheres, the fibers were modelled as consisting of several prolate spheroids connected through ball and socket joints. With prolate spheroids, the number of fiber components reduces compared to spheres, leading to faster simulations. On the other hand, ball and socket joints remove the possibility of stretching, which introduces the necessity of connection constraints, keeping the joints together. Ross and Klingenberg argued that extensibility could be neglected since it is typically small compared to other deformations. The bending and twisting torques of the ball and socket joints were governed by spring relations as in the model of Yamamota and Matsuoaka. The hydrodynamic force and torque acting on the spheroids were similar, and the governing equations of the spheroid motion were the same equations as Yamamota and Matsuoaka used, except that the joint constrains were included and the particle inertia was neglected.

Ross and Klingenberg used their model to simulate a single fiber in shear flow and compared the results to Forgacs and Mason [15, 16]. They also simulated multiple fibers and investigated rheological properties. When multiple fibers were used, a repulsive force between spheroids was employed.

In 1998, Stockie and Green [61] presented a new approach for simulation of fiber suspensions. They incorporated full two-way coupling between fiber and fluid by using the immersed boundary method by Peskin [51], and employed the Navier-Stokes equations to resolve the fluid motion. Their fiber model was fundamentally different from the previously described methods. A fiber was modelled as a flexible composition of force-bearing filaments, assumed to be massless and occupy zero volume. A force was introduced in the momentum equation of the Navier-Stokes equations which was non-zero except on the fiber. The fiber was forced to move at the same velocity as the surrounding fluid. By expressing the fiber density as the gradient of a potential function, resistance to stretching and bending was included. Stockie and Green used Hooke's law to govern the deformation of the fiber. The model was used to simulate a fiber in shear flow in two dimensions. The results showed some disagreement with previous simulations and theory, which all neglected the effect from the fibers on the fluid, indicating that this interaction is important.

In 2000 and subsequent years, Schmid, Switzer and Klingenberg [55,63,64]

published works similar to that of Ross and Klingenberg, but now with fibers that were modelled as composed of cylinders instead of prolate spheroids. Using this model they simulated several fibers in shear flow and investigated flocculation. In 2002, Stockie [60] extended his earlier model to three dimensions and investigated an elastic fiber in shear flow. The fiber was described using several layers and fibrils.

In 2007 and 2008, Lindström and Uesaka, published works [37, 38] where the fibers were built up of cylindrical elements, as in the work of Schmid and co-workers. Three new features compared to Schmid and co-workers were that the inertia of the elements was included, that the fluid flow was governed by the incompressible Navier-Stokes equations, and that two-way coupling was included. The two-way coupling was incorporated using boundary conditions derived by Hirasaki and Hellums [26]. Contact forces between fibers were also included, similar to the work of Yamamota and Matsuoka [70].

In 2011 and 2012, Mark and co-workers [41, 62] presented a new approach by modelling the fibers as beams governed by the Euler-Bernoulli beam equation in a co-rotational formulation. The fluid flow was governed by the Navier-Stokes equations, and a two-way coupling was included using a second-order accurate immersed boundary method [44]. The contact between fibers was modelled using a penalty method including elastic and inelastic collisions and friction. The fluid-fiber interaction was evaluated by simulating a fiber which was attached to a wall and exposed to a cross flow. Further fiber simulations were performed and compared with Jeffery's equations and the experimental results of Mason and co-workers.

In this thesis, the work of Mark and co-workers is extended to enable simulation of the paper forming process. A more advanced beam model is used and a novel fiber-fiber interaction model is developed. In the following sections, the four sub-models of the fiber suspension model are presented.

2.2   Fluid model

In this work, the fluid, in which the fibers are immersed, is governed by the Navier-Stokes equations, consisting of the momentum and the continuity equation

$$\rho\frac{\partial u}{\partial t} + \rho u \cdot \nabla u - \mu\nabla^2 u = -\nabla p,$$
$$\nabla \cdot u = 0. \tag{2.1}$$

where u is the fluid velocity, t is the time, p is the pressure, and ρ and μ are the density and dynamic viscosity of the fluid respectively.

The fluid flow is solved using the already existing incompressible finite-volume based fluid solver IBOFlow (Immersed Boundary Octree Flow Solver). The SIMPLEC method [11] is utilized to couple the momentum and pressure equations, and the fluid domain is discretized on a dynamic Cartesian octree grid. The octree grid structure permits fast refining and coarsening of the mesh. The variables are stored in a co-located configuration, and the Rhie-Chow interpolation [52] is adopted to suppress pressure oscillations.

IBOFlow is well-validated and is used in a wide range of applications in other projects. It is used for spay painting in the automotive industry with coupled simulations of air flow, electromagnetic fields and paint droplets [12, 39]. Moreover, IBOFlow is used for simulation of transient viscoelastic fluid flow [32], conjugate heat transfer [48], contact angles and surface wettabilities [19], and 3D bioprinting [20].

2.3   Object model

Two types of immersed objects are considered: fibers and forming fabrics. The fibers are modelled as beams using a finite-strain rod model developed by Simo and Vu-Quoc [57–59]. The model is a non-linear rod model including finite bending, shearing and extension, permitting deformations which are arbitrarily large in regard to rotation and strain. This is in contrast to the Bernoulli beam equations, which are only applicable to small deflections, more suitable for large static beams. The fabrics are considered rigid and static, and are represented by a surface triangulation or a volume mesh. The fabric geometries are scanned from real industrial fabrics.

To solve the fiber equations, Simo and Vu-Quoc used the finite element method in space together with Newton-Raphson iteration to handle the non-linearity. In time, they employed an implicit time stepping algorithm based on the Newmark scheme [47]. In this work, the time algorithm has been upgraded to an extension proposed by Ibrahimbegovic and Al Mikdad [30].

For the forthcoming presentation, it is worth remembering that each fiber is discretized into elements with nodes at the element end points. Each fiber is solved separately every time step and the size of the fiber time step is denoted Δt.

2.4 Fluid-object and object-fluid interaction model

The effect from the immersed objects on the fluid is handled by the second-order accurate immersed boundary method developed by Mark an co-workers [40, 44]. The hybrid mirroring immersed boundary method constrains the fluid velocity to the velocity of the immersed surface by an implicit boundary condition. A fictitious velocity field is created inside the body, which is excluded from the continuity equation to ensure zero mass flux over the boundary.

The effect from the fluid on the fibers is calculated by an empirical drag force relation derived from experiments. The drag force per unit length, f_D, acting on a fiber is assumed to be given by the expression

$$f_D = \frac{1}{2}\rho C_D \bar{d} |v^{\text{rel}}| v^{\text{rel}}, \tag{2.2}$$

where C_D is the drag coefficient, $\bar{d}$ is the mean diameter of a fiber cross section, and v^{rel} is the relative velocity of the fiber and fluid calculated at the center of the fiber cross section. The drag coefficient is calculated according to

$$C_D = \begin{cases} \dfrac{9.689}{Re^{0.78}}\left(1 + 0.147Re^{0.82}\right), & \text{if} \quad Re < 5, \\[2mm] \dfrac{9.689}{Re^{0.78}}\left(1 + 0.227Re^{0.5}\right), & \text{if} \quad Re \in [5, 40), \\[2mm] \dfrac{9.689}{Re^{0.78}}\left(1 + 0.0838Re^{0.82}\right), & \text{if} \quad Re \in [40, 400], \end{cases} \tag{2.3}$$

which originates from [54]. The Reynolds number is defined as

$$Re = \frac{\rho |v^{\text{rel}}| \bar{d}}{\mu}, \tag{2.4}$$

where μ is the dynamic viscosity of the fluid.

2.5 Object-object interaction model

When investigating suspension flows, it is customary to initially consider one single object immersed in a fluid. If self-contact is neglected, the three models presented in the preceding sections, the fluid model, the object model, and the fluid-object and object-fluid interaction model, are sufficient to describe the suspension flow. When multiple objects are immersed in a fluid, an additional phenomenon is introduced: the interaction between objects.

The interaction between immersed objects in a suspension becomes more

influential when the concentration increases. For dilute suspensions, the inter-
action can often be neglected. For higher concentrations, the effect can be of
major importance. High numerical cost and numerical instability are two diffi-
culties which have to be dealt with when modelling interaction between a large
number of objects.

Object interaction is usually calculated by using formulas for the contact
force between pair of objects. Such contact forces normally depends on the
surface separation in a way such that the force magnitude increases when the
surfaces are approaching, and eventually ends up in a singularity. This singu-
larity is one reason that could lead to numerical instability, especially when the
objects are moved in discrete steps each time step.

Another aspect of interaction forces is that physical and chemical forces,
for example those included in the DLVO theory [10, 65], the van der Waals and
electrostatic forces, are active on the nanoscale. These apparent variations over
small distances require the motion of the objects to be resolved with very small
time steps which is time-consuming.

In this work, a novel model for computing the interaction effects between
fibers, and fibers and fabric, is presented. The model is developed to resolve
contact forces acting at small scales without requiring the time step of the fiber
motion to be reduced. It includes a steric repulsion force adopted to, in a numer-
ically stable way, manage the repulsive forces acting on the smallest separation
distances where overlaps occur.

The model is based on so-called contact points which are distributed over
the fibers. Between these contact points the contact forces are calculated. The
force formulas used in this work are the DLVO forces together with the steric
repulsion force mentioned above. By solving the motion of the contact points
locally during each fiber time step, average forces can be calculated which are
added to the fibers and incorporated into the fiber beam equations.

2.5.1   Equation system for contact point motion

In this section, the system of ordinary differential equations governing the mo-
tion of the contact points is derived. A contact point is a moving point at which
a contact force is calculated.

Consider a fiber suspension with N objects at time t. For each object, a
number of contact points is chosen. Let the total number of contact points
for all objects be M, and for contact point i, denote its position, velocity, and
acceleration at time t by $p_i(t)$, $v_i(t)$, and $a_i(t)$, all belonging to $\mathbb{R}^3$, $1 \leq i \leq M$.
See Figure 2.2 for an illustration of fibers with contact points distributed along
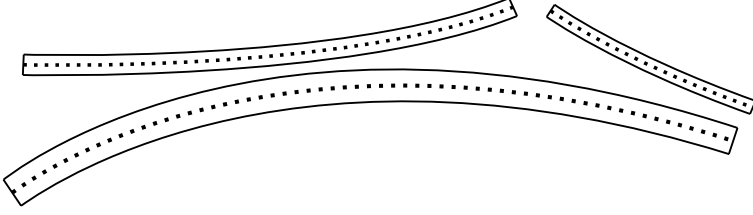the centerlines.

Figure 2.2: A two-dimensional illustration of three fibers and contact points distributed along the centerlines.

Combining the differential relation between position and acceleration, $\dfrac{d^2p}{dt^2} = a$, and Newton's second law, $F = ma$, the following differential equation for the position of contact point i is attained:

$$\frac{d^2p_i}{dt^2} = \frac{F_i}{m_i}, \tag{2.5}$$

where m_i denotes the mass related to contact point i, and F_i is the total force acting at position p_i. In this model, the following forces are considered to act on contact point i:

- F_i^G - The gravitational force.
- F_i^D - The drag force from the fluid.
- $F_{i,j}^I$ - The contact force from interaction with contact point j.
- $m_i a_{i,0}$ - The force from the intrinsic acceleration of the object, assumed to be constant during a fiber time step.

Inserting the forces into (2.5), results in the following system of second order differential equations:

$$\frac{d^2p_i}{dt^2} = a_{i,0} + \frac{1}{m_i}\left(F_i^G + F_i^D + \sum_{j \in J_i} F_{i,j}^I \right), \quad 1 \le i \le M, \tag{2.6}$$

where J_i is the set of indices of the contact points that contact point i interacts with.

The second order system (2.6) is rewritten as a first order system by intro-

ducing the variables

$$
y_i(t) = \begin{cases} p_i(t), & 1 \leq i \leq M, \\ v_{i-M}(t), & M+1 \leq i \leq 2M. \end{cases} \tag{2.7}
$$

This results in the following initial value problem for the motion of the contact points:

$$
\begin{cases} \dot{y}_i(t) & = y_{i+M}, \\ \dot{y}_{i+M}(t) & = a_{i,0} + \dfrac{1}{m_i}\left(F_i^G + F_i^D + \sum_{j \in J_i} F_{i,j}^I \right), \\ \begin{cases} y_i(t_0) & = p_i(t_0), \\ y_{i+M}(t_0) & = v_i(t_0), \end{cases} \end{cases} \quad 1 \leq i \leq M, \quad (2.8)
$$

where the initial positions and velocities of the contact points at time t_0 are given.

2.5.2   Calculation procedure

In this section, it is explained how the equation system (2.8) is used at each fiber time step during a simulation to calculate the interaction which is transformed into forces and moments that are added to the fiber equation. The system (2.8) is solved using the Adam-Moulton based ODE-solver SUNDIALS CVODE [25].

Given a time step at time t_0, contact points are distributed over the fibers (see Paper VI for details about the distribution). The velocity $v_i(t_0)$ and the intrinsic acceleration $a_{i,0}$, are extracted from the fibers at the position $p_i(t_0)$ for each contact point included in the equation system (see Section 2.5.3 for how the contact points included are chosen). The system is solved during the time step Δt, and the resulting positions of the contact points at time $t_0 + \Delta t$ are used to calculate an averaged force $\bar{F}_i$ using the Newmark-Wilson scheme [30]. The resulting force $\bar{F}_i$ is set to act at position $p_i(t_0)$. To include the force in the fiber equation, the force is transformed to the nodes of the fiber element which the contact point belongs to, such that the total force and moment acting on the fiber element are preserved, assuming rigidity of the element.

2.5.3   Simplification of equation system

The system of differential equations (2.8), governing the motion of the contact points will be very large if many fibers are considered. Solving such a large system is computationally demanding. Therefore, two simplifications are em-

ployed to reduce the size of the system.

In the simulations in this work, the system is solved only for pairs of contact points. Using this simplification, for a given contact point, the system is solved several times with different interacting contact points. This still implies a lot of calculations, most often between contact points whose interaction is very small. Hence one further simplification is used, which is, for a given contact point, to only solve the interaction with the closest contact point at each interacting fiber.

2.5.4   DLVO theory

The contact force between fibers, $F_{i,j}^I$, in equation system (2.8), is based on the DLVO theory. The DLVO theory (Derjaguin and Landau [10], Vervey and Overbeek [65]) describes force interactions between particles dispersed in a liquid. The idea of the DLVO theory is to calculate the total interaction through summation of forces arising from the following two separate phenomena:

- van der Waals forces,

- electrostatic forces.

Van der Waals forces are dipolar and multipolar forces. They are mostly attractive, while electrostatic forces are due to electric double layers and depend on the sign and magnitude of the surface charge of the interacting objects. While electrostatic forces are only non-zero when the surfaces are charged, van der Waals forces are present in almost all situations.

An example of a van der Waals force curve is shown to the left in Figure 2.3. The curve describes the force acting on a single object interacting with another object and depends on the surface separation distance. Negative values indicate attraction. As can be seen, the magnitude increases as the separation decreases. To the right in Figure 2.3, an electrostatic force curve is plotted for an object interacting with an equally charged object, and hence the value of the force is positive, which indicates repulsion.

In the DLVO theory, the two separate force contributions are added. To the left in Figure 2.4, the total DLVO force resulting from addition of the two forces in Figure 2.3 is plotted. It can be seen that at large separations, there is a small attractive force, but that its magnitude is very close to zero. When the objects get closer the attractive force becomes more significant. At a separation distance of about 3 nm the force changes sign. This point, where the force is zero, is called the secondary minimum, since the interaction energy is locally smallest there. It is a state of equilibrium, where the objects are stuck together at constant separation distance. However, a relatively small external force could
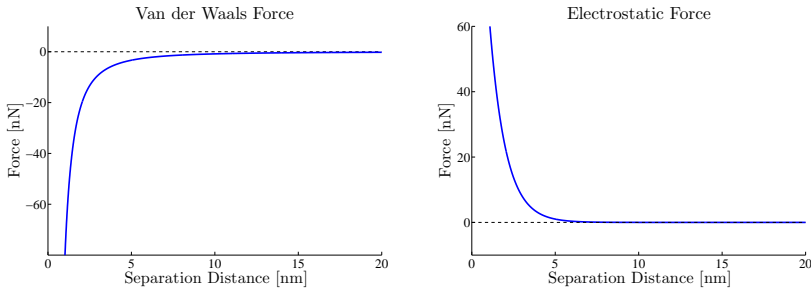
Figure 2.3: The two forces included in the DLVO theory. To the left the van der Waals force and to the right the electrostatic force.

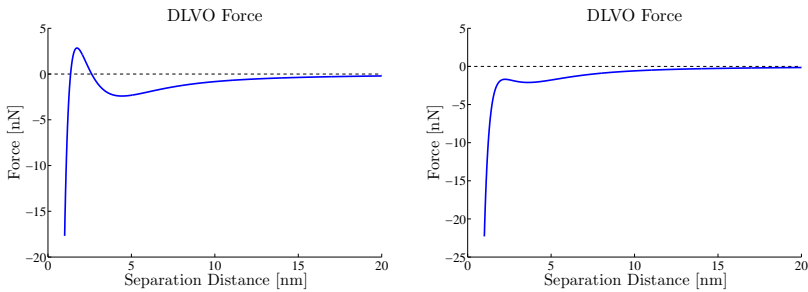separate two objects stuck in this minimum.

Figure 2.4: Graphs of DLVO forces acting on a single particle in contact with another particle. To the left, the forces in Figure 2.3 have been combined to a single DLVO curve. To the right, the resulting DLVO force is shown when the surface charge of the particles has been decreased.

To reach a stronger state of attraction between objects, the repulsive maximum at 2-3 nm has to be overcome. It is an attractive state called the primary minimum where a much larger force is required to separate the objects. The force curve to the left in Figure 2.4 indicates that objects closer than 2 nm will continue to attract and eventually collapse into each other. This is in reality prevented by steric repulsive forces arising from overlap of electron clouds. At sufficiently small separation distances the DLVO theory is not reliable.

If the surface charge of the objects is decreased, a resulting DLVO force curve could look like the one to the right in Figure 2.4. It can be seen that the repulsive hill no longer exists and therefore the objects stick together more easily.

Since the magnitude of the DLVO force is nonzero only at small surface distances, attraction will only occur if the particles are positioned very close to each other. In the following two sections, a description of the two DLVO force components, van der Waals and electrostatic, is presented.

2.5.4.1 Van der Waals contribution

Van der Waals interactions describe forces acting between atoms and molecules. These intermolecular interactions act on very small separation distances and are in most cases attractive. Van der Waals interactions are due to the three following types of forces:

- Keesom forces,

- Debye forces,

- London forces,

which all occur due to electrostatic interactions between molecular dipoles or multipoles and differ in whether the dipole or multipole is permanently or temporarily induced. The Keesom forces describe interactions between two permanent poles, London forces between two temporarily induced poles, and Debye forces between permanent and temporarily induced poles. Keesom and Debye forces can be analysed by electrostatic theory while London forces require quantum physics [1].

To calculate the resulting van der Waals forces on macroscopic objects, Hamaker [21] utilized the energy additivity principle by summation over all interacting atoms and molecules. In the case of two spherical objects, Hamaker [21] derived an expression for the energy which for $h/r_i \ll 1$ [1] reduces to

$$V_W = -\frac{A_{12}}{6h} \left(\frac{r_1 r_2}{r_1 + r_2} \right).$$ (2.9)

A force formula for the van der Waals interaction is obtained by the negative gradient of the potential, $-\dfrac{dV}{dh}$, which gives

$$F_W = -\frac{A_{12}}{6h^2} \left(\frac{r_1 r_2}{r_1 + r_2} \right).$$ (2.10)

The included parameters are the radii r_1 and r_2 of the two spheres, the surface separation distance h, and the Hamaker constant A_{12}. The Hamaker constant A_{ij} is a compact way of describing all constants involved in the van der Waals interaction.

2.5.4.2   Electrostatic contribution

In principle all surfaces get charged to some extent when immersed in a liquid media. The charging is usually due to one of three mechanisms, dissociation of ionic groups on the surface, adsorption of ions from the liquid medium, or quantum mechanical charge transfer between atoms in surfaces brought very close to each other. Irrespectively of charging mechanism, a so called electric double layer is created, consisting of the inner layer surface charge and a second layer of oppositely charged counterions [33]. The establishment of double layers enables electrical interactions between particle surfaces in liquids, eventually leading to repulsive and attractive forces between the particles.

A common starting point for calculations of interactions between particles in suspensions is the Poisson-Boltzmann equation. As this equation is non-linear and an analytical solution often is hard to find (except for simple cases such as that of two planar surfaces) a common method is to deal with the linearised version. It is also common to limit the work to the interaction between two spherical objects [1].

The introduction of approximations gives restrictions on the intervals in which the solution is valid. Bell et al. [4] have derived an approximate solution to the non-linear Poisson-Boltzmann equation for the interaction between two colloidal spheres, resulting in

$$F_E = 4\pi\varepsilon \left(\frac{kT}{e}\right)^2 \bar{Y}_1^0 \bar{Y}_2^0 \frac{r_1 r_2}{R^2} \cdot (1 + \kappa R)e^{-\kappa(R - r_1 - r_2)}, \qquad (2.11)$$

where F_E is the force due to interaction between the two spheres, ε the permittivity of the liquid medium, k the Boltzmann constant, and T the absolute temperature of the solution. Moreover, r_i, $i \in \{1, 2\}$, are the radii of the first and second sphere respectively, R is the distance between the centers of the spheres, $\bar{Y}_i^0$ is the effective surface potential, e is the elementary charge, and κ is the inverse of the Debye length. This solution is valid for any potential but only for distances between the spheres satisfying $\kappa(R - r_1 - r_2) > 1$. The Debye length $1/\kappa$ is a property of the electric double layer describing how far out from the surface the electrostatic effects are significant. It is a property dependent only on the liquid solution and not on the surface charge [33]. An approximate formula for the effective surface potential of a spherical double layer in a 1:1 electrolyte (consisting of equally many ions of valency $+1$ as -1)

is found in [1] as

$$\bar{Y}_i^0 = \frac{8 \tanh\left(\dfrac{e\psi_{d,i}}{4kT}\right)}{1 + \left[1 - \dfrac{2r_i\kappa + 1}{(r_i\kappa + 1)^2} \tanh\left(\dfrac{e\psi_{d,i}}{4kT}\right)\right]^{1/2}}. \tag{2.12}$$

The diffuse double layer potential $\psi_{d,i}$ is unknown in (2.12). It is common that the surface charge σ_i^0 is known but not the diffuse double layer potential. A relation between the two quantities reads [1]

$$\sigma_i^0 = 2\sinh\left(\frac{e\psi_{d,i}}{2kT}\right) + \frac{4}{\kappa r_i} \tanh\left(\frac{e\psi_{d,i}}{4kT}\right), \tag{2.13}$$

from which $\psi_{d,i}$ can be found by iteration, and hence $\bar{Y}_i^0$ and the force in (2.11) can be calculated.

2.5.4.3 Extension of DLVO forces

The DLVO force formulas are inaccurate at the smallest separations and they diverge towards negative infinity when the separation goes to zero. The formulas are therefore not used for separation distances smaller than h_0. To get a smooth translation at $h = h_0$, the formulas are extended to $h = 0$. For the van der Waals and electrostatic forces, two splines are used to smoothly let the function reach zero at zero separation. The new formulas have the forms

$$F_W(h) = \begin{cases} -\dfrac{A_{12}}{6h^2}\left(\dfrac{r_1 r_2}{r_1 + r_2}\right), & h \geq h_0, \\ g_W(h), & h < h_0, \end{cases} \tag{2.14}$$

$$F_E(h) = \begin{cases} 4\pi\varepsilon\left(\dfrac{kT}{e}\right)^2 \bar{Y}_1^0 \bar{Y}_2^0 \dfrac{r_1 r_2}{R^2}(1 + \kappa R)e^{-\kappa(R - r_1 - r_2)}, & h \geq h_0, \\ g_E(h), & h < h_0. \end{cases} \tag{2.15}$$

The functions, $g_i(h)$, $i \in \{E, W\}$, are defined as

$$g_i(h) = \begin{cases} 0, & h \leq 0, \\ a_i h^2, & 0 \leq h < \dfrac{h_0}{2}, \\ b_i h^2 + c_i h + d_i, & \dfrac{h_0}{2} \leq h < h_0, \end{cases} \tag{2.16}$$

where the constant coefficients a_i, b_i, c_i and d_i are chosen such that

$$F_i \left(\frac{h_0}{2} \right) = g_i \left(\frac{h_0}{2} \right),$$

$$F_i' \left(\frac{h_0}{2} \right) = g_i' \left(\frac{h_0}{2} \right),$$

$$F_i(h_0) = g_i(h_0),$$ (2.17)

$$F_i'(h_0) = g_i'(h_0).$$

This choice guarantees smoothness preventing unstable behaviour. The resulting coefficients can be seen in the Appendix of Paper VI.

The extension of the van der Waals and electrostatic formulas are plotted in Figure 2.5 to the left and right, respectively. Adding these two extended force formulas results in the extended DLVO force illustrated in Figure 2.6.
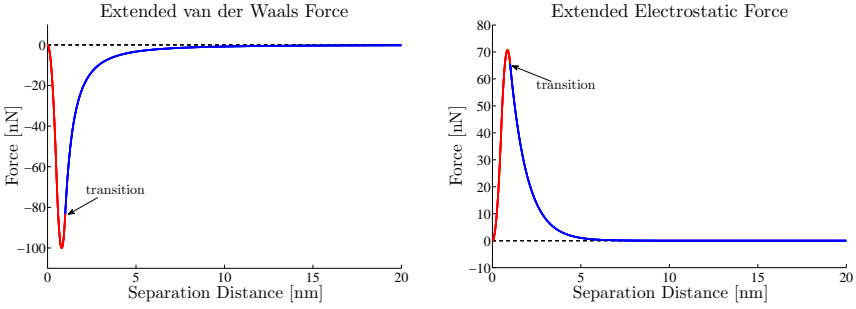
Figure 2.5: The theoretical van der Waals and electrostatic formulas only apply at separation distances larger than h_0. The formulas are therefore extended using splines to smoothly reach zero at zero separation distance. The transitions between the curves are marked with arrows.

Figure 2.6: The curves in Figure 2.5 are added to form a total DLVO force curve. The sum of the extensions is shown in red and the sum of the theoretical curves in blue. The transition between the curves is marked with an arrow.

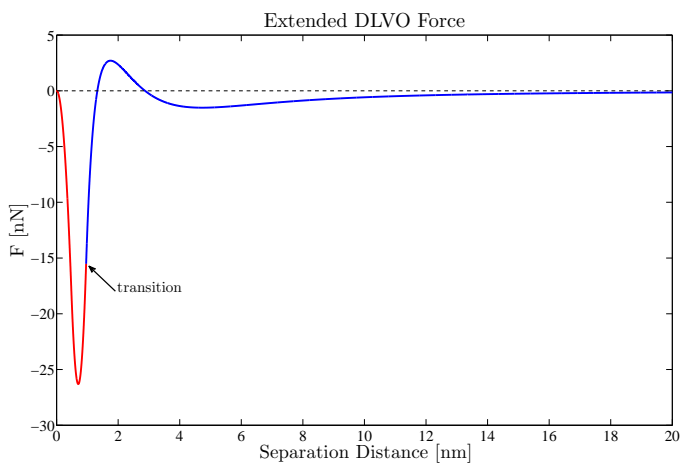## 2.5.5 Steric repulsion force

In addition to the DLVO forces, a steric repulsion force is included in the interaction force between fibers, $F_{i,j}^I$. The purpose of the steric repulsion force, F^S, is to prevent objects from passing into each other and to repel objects that overlap. Since the simulation framework uses discrete time stepping, fibers can partially overlap after a time step. This constitutes extra requirements on the construction of a numerically stable steric repulsion force. The force developed in this work consists of four different forces according to

$$F_S = \sum_{i=1}^{4} F_{S,i}, \tag{2.18}$$

and they are only nonzero for separations $h < h_0$. The four forces are given by

$$F_{S,1} = \max\left(0, B_1 \frac{2}{t_R^2} \frac{h_R - h - t_R \tilde{v}_{\text{rel}}}{\frac{1}{m_1} + \frac{1}{m_2}}\right), \tag{2.19}$$

$$F_{S,2} = B_2 \frac{\tilde{v}_{\text{rel}}|\tilde{v}_{\text{rel}}|}{h_S \left(\frac{1}{m_1} + \frac{1}{m_2}\right)}, \tag{2.20}$$

$$F_{S,3} = B_3 \frac{\tilde{v}_{\text{rel}}|\tilde{v}_{\text{rel}}|}{\frac{h_{\min}}{1000}\left(\frac{1}{m_1} + \frac{1}{m_2}\right)}, \tag{2.21}$$

$$F_{S,4} = B_4 \frac{\tilde{v}_{\text{rel}}|\tilde{v}_{\text{rel}}|}{h_S \left(\frac{1}{m_1} + \frac{1}{m_2}\right)}. \tag{2.22}$$

The functions $B_i = B_i(h)$, $i = 1, 2, 3, 4$, are bell-like with the purpose of constraining the action of the forces to certain separation distances. The explicit forms of the bell functions can be seen in the Appendix of Paper VI. The masses of the two contact points are denoted m_1 and m_2, and $h_{\min} = -r_1 - r_2$, where r_1 and r_2 are the two representative radii of the contact points. The separation $h_{\min}$ represents the minimum possible separation distance before the points pass through each other.

The scalar valued function $\tilde{v}_{\text{rel}}$ is the relative velocity of the contact points projected onto the direction vector $\hat{n}$:

$$\tilde{v}_{\text{rel}} = -\hat{n} \cdot v_{\text{rel}}, \tag{2.23}$$

where $v_{\text{rel}} = v_2 - v_1$. The direction vector is a unit vector pointing between the contact points, directed away from the contact point considered. The dis-

tances h_R and h_S are separations chosen as fixed parameters. Similarly t_R is a reference time.

The first force, $F_{S,1}$, acts at separations $h < h_R$ and the instantaneous value is calculated such that the separation will be equal to h_R in time t_R neglecting all other forces and velocities. The value is also adjusted to not give any attraction but only repulsion. This force acts to separate contact points.

The second force, $F_{S,2}$, prevents contact points from reaching a separation $h = -r_1 - r_2$, that is, to prevent them from passing through each other. The third and fourth force, $F_{S,3}$ and $F_{S,4}$, both damp the velocities of the contact points when they are moving away from each other so that the repulsive velocity that is built up during the intersection stage will not lead to that the DLVO forces are being ignored.

2.6   Testing of object-object interaction model

In this section, some basic testing of the object-object interaction model is presented. Two test cases have been studied, one where two parallel fibers collide, and one where two parallel fibers pass each other with a slight touch. In the first case, it is investigated whether the contact model can handle head-on collision, and in the second case, the adhesive contribution from the van der Waals force is investigated.

2.6.1   Collision test

In the collision test, two cylindrical fibers with length $L = 0.1$ mm and diameter $D = 14\,\mu$m are positioned in parallel to the y-axis in the x-y-plane with an initial surface separation of $h = 12\,\mu$m. One of the fibers is held moving at a constant speed of $v = 50$ mm/s in direction towards the other fiber. The fibers collide and the moving fibers pushes the other fiber forward. This is illustrated in Figure 2.7.

(a) $t = 0.0$ ms.   (b) $t = 0.2$ ms.   (c) $t = 0.4$ ms.   (d) $t = 1.0$ ms.
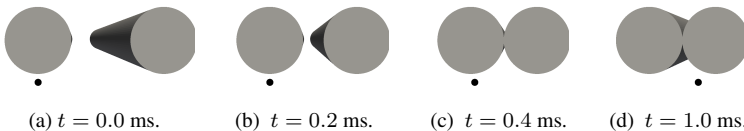
Figure 2.7: Collision between two cylindrical fibers. The right fiber is moving with a constant speed of $v = 50$ mm/s to the left. The black dot is a static reference point.

2.6.2   Adhesion test

In the adhesion test, two cylindrical fibers with length $L = 0.1$ mm and diameter $D = 14\,\mu$m are positioned in parallel to the y-axis in the x-y-plane with an initial surface separation of $h = 12\,\mu$m. One fiber is translated $\Delta z = 12\,\mu$m in the direction of the z-axis and is held at a constant speed v in the x-direction towards the other fiber. The two fibers touch each other, and depending on the speed, the adhesion becomes long-lived or short-lived. For $v = 10$ mm/s the adhesion becomes long-lived and for $v = 50$ mm/s short-lived. This can be seen in Figure 2.8 for the case of $v = 10$ mm/s and in Figure 2.9 for the case of $v = 50$ mm/s .

(a) $t = 0.0$ ms.   (b) $t = 0.5$ ms.   (c) $t = 1.0$ ms.   (d) $t = 1.5$ ms.   (e) $t = 2.0$ ms.

(f) $t = 2.5$ ms.   (g) $t = 3.0$ ms.   (h) $t = 3.5$ ms.   (i) $t = 4.0$ ms.   (j) $t = 4.5$ ms.

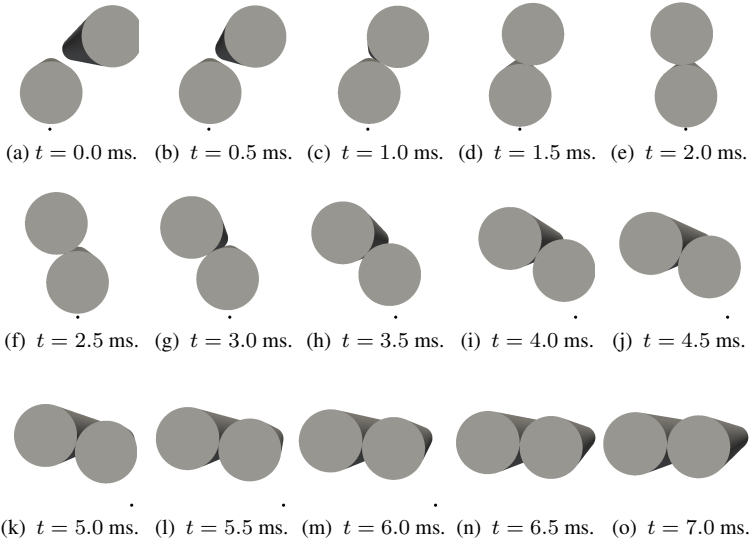(k) $t = 5.0$ ms.   (l) $t = 5.5$ ms.   (m) $t = 6.0$ ms.   (n) $t = 6.5$ ms.   (o) $t = 7.0$ ms.

Figure 2.8: Long-lived adhesion after partial collision between two cylindrical fibers. The originally right fiber is moving with a constant velocity $v = 10$ mm/s to the left. The black dot is a static reference point.

(a) $t = 0.0$ ms.   (b) $t = 0.2$ ms.   (c) $t = 0.3$ ms.   (d) $t = 0.4$ ms.   (e) $t = 0.5$ ms.

(f) $t = 0.6$ ms.   (g) $t = 0.7$ ms.   (h) $t = 0.8$ ms.   (i) $t = 0.9$ ms.   (j) $t = 1.3$ ms.
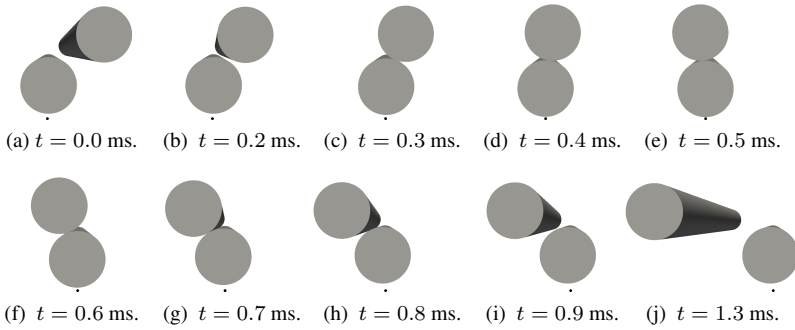
Figure 2.9: Short-lived adhesion after partial collision between two cylindrical fibers. The fiber which is originally located to the right is moving with a constant velocity $v = 50$ mm/s to the left. The black dot is a static reference point.

3. Paper Forming Simulation Framework

The motivation behind the suspension flow model presented in the preceding chapter was to enable simulation of the lay down process in the forming section of a paper machine. In the forming section, a fiber suspension, consisting of paper pulp diluted into water, is injected through the head box. The suspension flows down onto a forming fabric moving at high speed, and the paper structure starts to form while most of the water passes through the holes of the fabric.

By implementing the suspension model presented in Chapter 2 into the fluid solver IBOFlow, a framework has been created that can be used to simulate the process described. In this chapter, the different parts of the framework are presented. The lay down simulations are performed with a domain fully filled with a fluid into which fibers are generated. At the lower part of the domain a small piece of an industrial forming fabric is held static and the fluid is accelerated over the fabric by an applied pressure drop. The resulting flow moves the fibers downwards onto the fabric and a paper sheet is build up.

An additional feature that is included is a method to press the fiber structure by letting a rigid plane move at constant velocity down onto the web, forcing the fibers together and decreasing the thickness of the sheet.

In Section 3.1, the setup of the simulation domain is described, and in Section 3.2, the simulation procedure is outlined. Thereafter, the forming fabric is presented in Section 3.3, and in Section 3.4, the pressing approach is explained. Lastly, some results from the lay down simulations are given.

3.1   Simulation domain

The simulation domain is an axis-aligned rectangular box whose horizontal pla-
nar dimension is equal to the dimension of the piece of forming fabric. A piece
of 3×3 mm^2 is used in the simulations. The height of the domain is adapted
to the number of fibers generated. The forming fabric is positioned with its
lower side 2 mm from the bottom of the domain. A snapshot of the domain
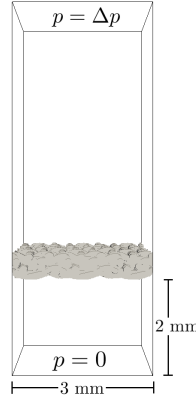with forming fabric is shown in Figure 3.1.

Figure 3.1: The simulation domain used for the lay down simulations. At a
distance of 2 mm from the bottom, a 3×3 mm^2 piece of a forming fabric is
held static. A pressure drop accelerates the fluid in the domain.

The domain contains a fluid which is accelerated by a pressure drop across
the domain in the vertical direction. This setup, with a domain constantly filled
with a fluid resembles the film that is present in the real process. The fluid
flow is determined by the following boundary conditions: at the four vertical
boundaries a symmetry boundary condition is used, that is,

$$\frac{\partial v_i}{\partial x_j} = 0, \quad i \in \{1, 2, 3\},$$
$$\frac{\partial p}{\partial x_j} = 0,$$

(3.1)

where $j \in \{1, 2\}$ depends on the boundary considered. At the top boundary,
the pressure is set fixed and the velocity is governed by a Neumann condition

in the following way:

$$\frac{\partial v_i}{\partial x_3} = 0, \quad i \in \{1, 2, 3\},$$
$$p = \Delta p,$$
(3.2)

where Δp is a prescribed pressure drop. Similarly for the bottom boundary:

$$\frac{\partial v_i}{\partial x_3} = 0, \quad i \in \{1, 2, 3\},$$
$$p = 0.$$
(3.3)

To prevent fibers from falling off the fabric at the boundaries of the domain, a cyclic boundary condition for the contact detection is used. Fibers close to one side detect fibers that are close on the opposite side. See Figure 3.2 for an illustration of the cyclic boundary condition for fiber-fiber contact.
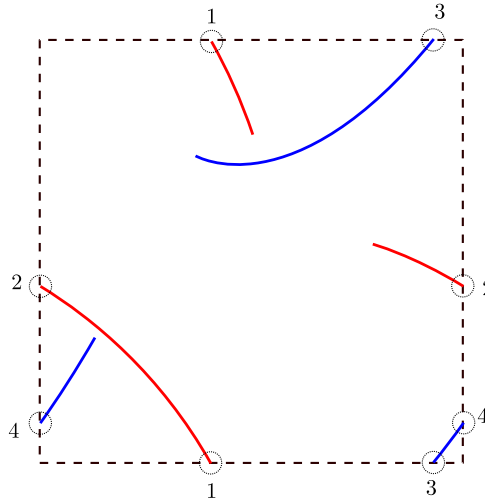

Figure 3.2: Illustration of how the fiber geometries are interpreted cyclically for the fiber-fiber interaction calculation. The simulation domain is viewed from above and two fibers are included, showing how they are represented when going out over the boundary.

3.2   Simulation procedure

The procedure of a paper forming lay down simulation is as follows:

1. The forming fabric is loaded into the simulation domain.

2. Fibers are randomly generated into the simulation domain.

3. Time stepping:

   (a) The fluid flow is computed by solving the Navier-Stokes equations resolving the object-fluid interaction by the immersed boundary method.

   (b) The interaction between fibers are solved locally using the fiber-fiber coupling model.

   (c) The resulting object-object interaction is transformed into forces and torques, which are added to the fiber equation.

   (d) The motion of the fibers is calculated using the fiber model.

If one-way coupling is used, which means that the fluid affects the fibers, but the fibers do not affect the fluid, step 3 (a) only has to be performed once. In that case, only the fluid flow over the forming fabric is resolved, and the fluid flow can be loaded from file directly at the beginning of the simulation, which saves substantial time. If fully two-way coupling is used, step 3 (a) is performed in each time step. Other approaches are to update the fluid flow not every time step but more seldom, or to only include fibers that are close to the fabric when calculating the effect on the fluid. For a description of the fiber generation, see Paper VI.

3.3   Forming fabric

The forming fabric used in the lay down simulations is a 3×3 mm^2 piece of a PRINTEX Q13 eight-shed double layer fabric from Albany International [1]. The height of the fabric is 0.637 mm. The geometry of the fabric is generated from tomography images and described numerically by a triangulation. In Figure 3.3 the forming fabric is visualized.

When calculating the interaction between fibers and fabric the contact points on the fabric are chosen in the following way: for a given contact point on a fiber, the closest node of the fabric triangulation is found. If this point is close enough to the contact point of the fiber, the surface normal at the closest point
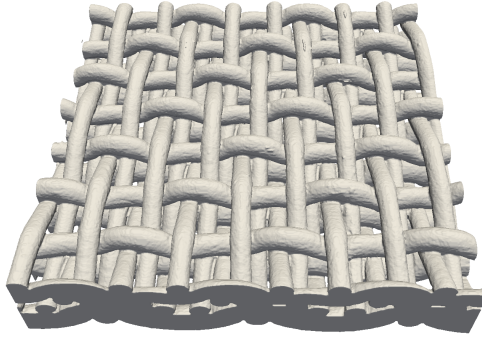
---

[1]http://www.albint.com/en-us/Pages/default.aspx

Figure 3.3: A 3×3 mm^2 piece of a forming fabric represented by a triangulation.

on the triangulation is used to define a plane. The closest point in this plane is used as interacting contact point.

3.4 Pressing

In the pressing section of a paper making machine, the paper sheet is pressed between large rolls under high pressure. In this simulation framework, a simplified approach of pressing has been employed.

After a lay down simulation, when the paper sheet has formed on the forming fabric, the velocity field of the fluid is set to zero, and a horizontal rigid plane is inserted. The plane moves downward at constant velocity to compact the sheet structure. In the current implementation, no force is driving the plate, and no resulting force from the fibers is calculated. Therefore at some point the plate will force the fibers together so much that they start to intersect unrealistically. Hence it is manually chosen when the pressing is finished.

The interaction between fibers and the plane is calculated similarly as to the interaction with the forming fabric. For each contact point on a fiber, the closest point on the press plate is used as the interacting contact point.

3.5 Lay down simulations

The simulation framework is used to simulate lay down of paper sheets with different density and the resulting virtual sheets are compared to experiments by simulating the air flow through the sheets. In this section, a review of the simulation results is presented. For a complete presentation of the simulation parameters, the experimental setup and the simulation results, see Paper VI.

The simulations are performed using one-way coupling, meaning that the fibers do not affect the fluid. With this simplification, the fluid flow over the fabric alone is initially simulated to steady state. The resulting flow field is used during the whole lay down process. This simplification drastically reduces the simulation time since two-way coupling is very expensive. However, the self-healing phenomenon taking place during the real forming process, where the fluid flow is continuously changing when fibers lay down, is not taken into account. Hence, the comparison between experiments and simulations gives indications about the influence of this effect.

The lay down simulations are performed for two different types of fibers, fibers with circular fiber cross-section and fibers with rectangular fiber cross-section. For each case, the injection mass is varied. Thereafter the sheets are pressed. The air flow through the sheets and fabric is simulated before and after pressing. The thickness of the sheets at the various stages has been calculated.

In Figure 3.4, images of two experimental sheets with different amounts of fibers are shown. In Figure 3.5, snapshots of two virtual sheets are shown. One sheet has circular fiber cross-section and the other rectangular fiber cross-section. Two snapshots of the air flow through fabric and virtual sheet are shown in Figure 3.6. Lastly, in Figure 3.7, the air permeability and thickness of the virtual and experimental sheets are plotted.

| (a) | (b) |

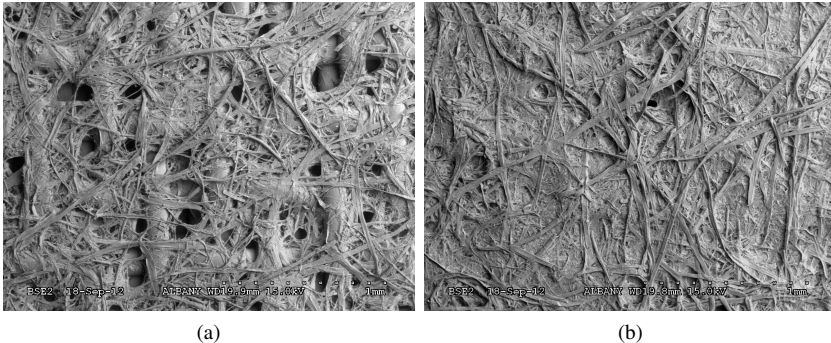Figure 3.4: SEM-images of two experimental sheets with different amount of fibers. The real size of the images are approximately 2.6×1.9 mm^2. Pictures courtesy of Albany International.

The snapshots of the virtual sheets show the three-dimensional network structure that can be created using the proposed simulation framework. The air flow simulations can help to increase the understanding of how the flow is

changing during the initial formation of paper sheets. The air permeability results show that the simulation and experimental values agree well for the sheets with lowest density, indicating the capacity of the fluid solver to simulate flow through forming fabrics. For sheets with higher densities, the permeability of the experimental sheets are lower than for the virtual sheets. This is believed to be explained by the one-way coupling simplification, leading to reduced amount of fibers staying on the fabric and in the sheet, since the flow field is not reduced the way it would be if the flow was continuously resolved when the fibers accumulate during lay down. Moreover, the discrepancy in permeability may also be caused by too weak adhesion in the contact model or too low conformability between fibers. The latter referring to how easily fibers deform over each other, reducing the porosity of the sheet. However, both two-way coupling and increased conformability should improve the conditions for adhesion.

(a) Circular fiber cross-section.   (b) Rectangular fiber cross-section.
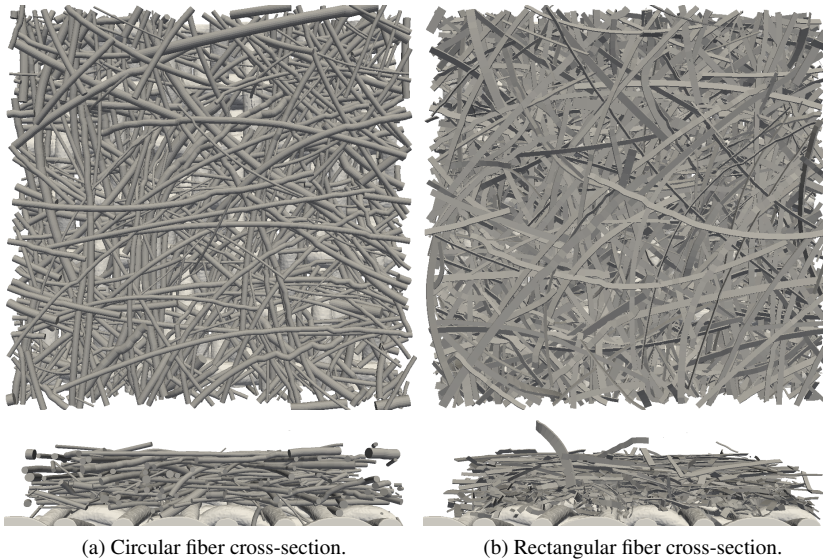
Figure 3.5: Snapshots from above and from side of two simulated paper sheets. One sheet with circular fiber cross-section and one sheet with rectangular fiber cross-section are included.

(a) Unpressed rectangular.

(b) Pressed rectangular.

Figure 3.6: Velocity magnitude field slices from air flow simulations through fabric and virtual sheet with rectangular fiber cross-section, before and after pressing. The slices are parallel to the x-z-plane. The width of each snapshot is 1 mm.

(a) Volume flow per area.

(b) Thickness.

Figure 3.7: The volume flow per area and thickness of the virtual and experimental paper sheets.

4. Flow over Forming Fabrics

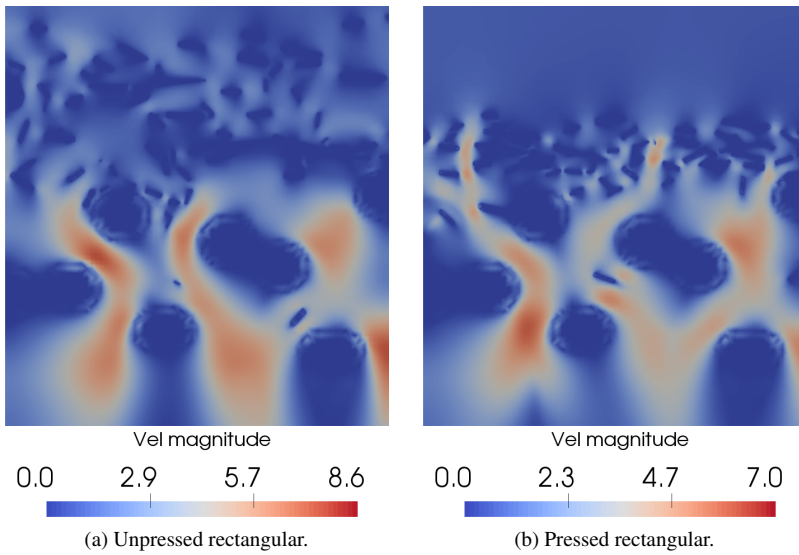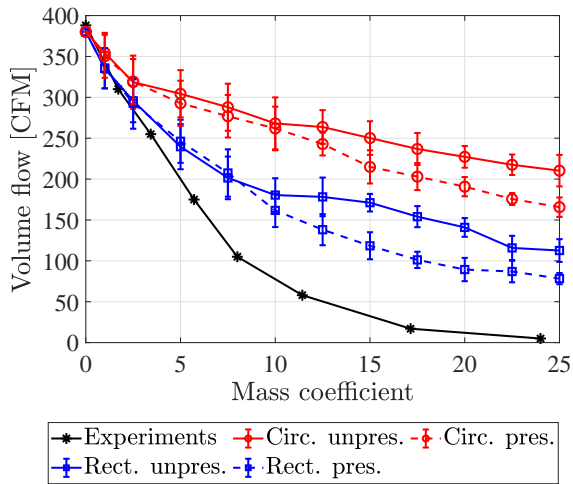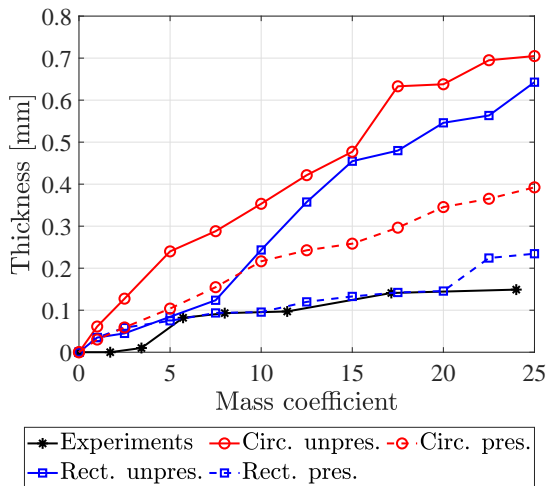The basic structure of the final paper product is formed during the lay down process in the forming section. The lay down is governed by the flow conditions, which effect how the fibers flow down onto the forming fabric. The structure of the woven fabric directly affects the flow and the formation of the fiber network configuration. Therefore, investigation of the fluid flow in the forming section and how it is affected by the fabric structure can help to improve the process and the paper structure. In this work, the fundamentals of upstream flow over forming fabrics are studied.

To attain a fundamental understanding of the flow over fabrics, the flow over various cylinder configurations is simulated, representing a simplification of the fabric structure. The flows over one cylinder, two cylinders, and one and two rows of cylinders are investigated numerically. Uniform cylinder diameters and uniform spacing between cylinders are assumed to reduce the number of possible configurations. The Reynolds number and the cylinder spacing are altered to investigate their effect on the upstream flow features.

To characterize the impact on the upstream flow from the different cylinder configurations and forming fabrics, new measures of the flow impact from the structure are proposed. These measures can be used for characterization of fabrics, in addition to the classic CFM-measure which gives a value of the air flow per area through a fabric at a certain pressure drop. The new measures quantify how far upstream the mainstream velocity is affected by the fabric and how large the deviations from the mainstream velocity are.

Lastly, the flow over three industrial forming fabrics are investigated numerically. The proposed impact measures are applied and conclusions are drawn based on findings in the cylinder study. Moreover, the flow patterns over the

fabrics are analysed and related to drainage marking.

In Section 4.1, the study of the flow over cylinders is presented. In Section 4.2, the proposed flow impact measures are described. In Section 4.3, the investigation of flow over three industrial forming fabrics is summarized. Lastly, some main results from the flow simulations are given.

4.1   Flow over cylinders

In this work, the upstream flow over cylinders is studied to increase the understanding of the flow over forming fabrics. Rows of cylinders constitute a two-dimensional simplification of the fabric structure. Such a two-dimensional setup enables basic investigation of the flow dependency of parameters such as the Reynolds number and the cylinder surface spacing. Flow over cylinders has been studied for a long time. Most studies focus on the downstream flow features and wake behaviour, in particular for the high Reynolds number regime. The majority of the studies consider the flow over one and two cylinders. In this work, flows over rows of cylinders are simulated, and the emphasis is on the upstream flow features in the Reynolds numbers regime 10-80, which is a typical condition in the forming section of a paper machine [18].

First, the flows over one and two cylinders are simulated to clarify the upstream flow features of the base case of one cylinder and how it is changed when one additional cylinder is added. Thereafter, the flow over one row of cylinders is investigated, and finally the flow over two rows. The cylinder diameter, d, is assumed to be the same for all cylinders and the Reynolds number is defined as

$$Re = \frac{\rho V_0 d}{\mu},\tag{4.1}$$

where ρ is the fluid density, μ is the fluid dynamic viscosity, and V_0 is the mainstream velocity. The two-dimensional simulations are performed in the x-y-plane and the cylinders are positioned parallel to the z-axis. The simulation domain for the flow over two cylinders is depicted in Figure 4.1. At the upper boundary, the v-velocity is prescribed to V_0 in the negative y-direction and the pressure is set by a Neumann condition. Symmetry conditions are used at the boundaries parallel to the y-axis, with Neumann conditions for both velocity and pressure. At the lower boundary, the pressure is set to zero and the velocity is prescribed by a Neumann condition. For the simulations with rows of cylinders, a cyclic domain is used in the x-direction with cyclic boundary conditions.

For the case of two cylinders, two configurations are studied, tandem and
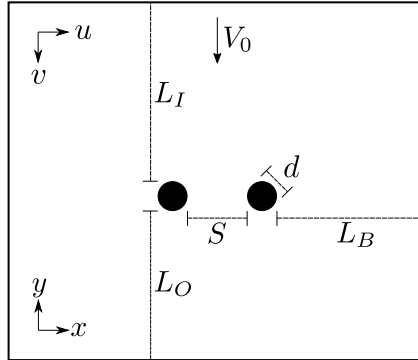
Figure 4.1: The two-dimensional simulation domain for the flow over two cylinders positioned side-by-side.
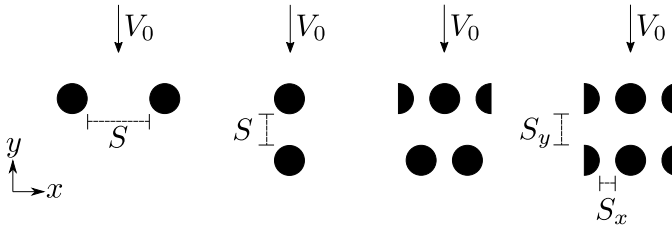
Figure 4.2: The two cases of two cylinders and two rows of cylinders and their respectively configurations. From left to right: two cylinders side-by-side, two cylinders tandem, two rows displaced, and two rows tandem.

side-by-side. For the case of two rows of cylinders, similarly two configurations are studied, one where the second row is placed in tandem and one where the second row is displaced half the surface spacing. These different configurations are shown in Figure 4.2. The position $y = 0$ corresponds to the top surface of the uppermost cylinders. The spacing between cylinder surfaces are denoted S. For two rows of cylinders, two spacings are relevant, the spacing between the cylinders in one row and the spacing between the two rows. To clarify which spacing is concerned, the notation S_x and S_y is used. If subindex x is used, the spacing parallel to the x-axis is considered, and analogously for subindex y.

The normalized spacings are denoted g and l, defined as

$$g = \frac{S_x}{d},$$
$$l = \frac{S_y}{d}. \tag{4.2}$$

The resulting flow simulations are analysed in terms of the velocity field with x-velocity denoted u and y-velocity denoted v. Note that the v-velocity is defined to be positive in the negative y-direction, as indicated in Figure 4.1. Three types of velocity plots are investigated: velocity profiles, extreme velocity functions, and level curves. The normalized velocity profiles are the functions

$$\frac{v(x, C)}{V_0} \quad \text{and} \quad \frac{u(x, C)}{V_0}, \tag{4.3}$$

where C is a fixed y-position upstream. The extreme velocity functions are the maximum and minimum values of the velocity profiles, defined as

$$M_v\left(\frac{y}{d}\right) = \max_{x \in W} \frac{v(x, y)}{V_0},$$
$$m_v\left(\frac{y}{d}\right) = \min_{x \in W} \frac{v(x, y)}{V_0}, \tag{4.4}$$
$$M_u\left(\frac{y}{d}\right) = \max_{x \in W} \frac{|u(x, y)|}{V_0},$$

where $W = [-w, w]$ for some large value of w, for example the width of the simulation domain. The level curves are sets of points which fullfill one of the two conditions

$$\frac{v(x, y)}{V_0} = C \quad \text{or} \quad \frac{|u(x, y)|}{V_0} = C, \tag{4.5}$$

depending on if the v- or u-velocity is considered.

4.2   Impact measures

To be able to compare the upstream flow impact between the various cylinder configurations and different types of forming fabrics, general measures are practical. One such measure is the CFM-value of a fabric, defined as the volume flow of air per area (in feet per minute) for a given pressure drop, e.g. 125 Pa. However, the CFM-measure and other measures used in the paper making industry, are not enough to characterize different types of fabrics in terms of

flow properties [36]. In this work, new measures are proposed that can be used to improve the characterization of forming fabrics.

Three types of impact measures are proposed. First, a measure that specifies how far upstream from the structure the mainstream velocity is affected more than a given threshold. Second, a measure that quantifies how large the variation between the maximum and minimum values of the velocity components is at different positions upstream. Third, a measure that gives the total area upstream where the structure influences the mainstream velocity more than a threshold value. The two first measures are used both for the simulations of the flow over cylinders and forming fabrics, while the area-measure only is applied to the two-dimensional cylinder simulations. An extension of the area-measure to fabrics is left for future work.

To strictly define the three measures, the following two indicator functions are used:

$$I_a^v \left(\frac{x}{d}, \frac{y}{d} \right) = \begin{cases} 1, & \text{if} \quad \left| \dfrac{v(x,y)}{V_0} - 1 \right| \geq a, \\ 0, & \text{else,} \end{cases} \tag{4.6}$$

$$I_a^u \left(\frac{x}{d}, \frac{y}{d} \right) = \begin{cases} 1, & \text{if} \quad \left| \dfrac{u(x,y)}{V_0} \right| \geq a, \\ 0, & \text{else.} \end{cases} \tag{4.7}$$

The area-measure, $A_a^\Gamma, \Gamma \in \{u, v\}$, is defined according to

$$A_a^\Gamma = \frac{1}{n} \iint\limits_{W \times \mathbb{R}_+} I_a^\Gamma (s, t) \, ds dt, \tag{4.8}$$

where n is the number of cylinders in the periodic domain of width nd. Notice that the area-measure is normalized such that $A_a^\Gamma = 1$ corresponds to an area of d^2.

The length-measure, $L_a^\Gamma, \Gamma \in \{u, v\}$, is defined as

$$L_a^\Gamma = \sup \left\{ \frac{y}{d} : I_a^\Gamma \left(\frac{x}{d}, \frac{y}{d} \right) = 1 \text{ for some } x \in \mathbb{R}_+ \right\}, \tag{4.9}$$

giving the highest normalized y-position where the flow deviates at least a portion a away from the mainstream velocity V_0.

Finally, the variation-measure D^Γ, $\Gamma \in \{u, v\}$, is defined as

$$D^v \left(\frac{y}{d} \right) = \max_{x \in \mathbb{R}} \frac{v(x,y)}{V_0} - \min_{x \in \mathbb{R}} \frac{v(x,y)}{V_0}, \tag{4.10}$$

$$D^u \left(\frac{y}{d} \right) = \max_{x \in \mathbb{R}} \frac{|u(x,y)|}{V_0}, \tag{4.11}$$

and measures the difference between the highest and lowest value of the velocity profiles at an upstream position y/d. Note that the variation-measure for the u-velocity gives the maximum magnitude of the velocity. The variation-measure can be related to the length-measure by, for a certain threshold value a, calculating the variation-measure at the resulting upstream position L_a^v, given by the length measure. That is:

$$D_a^v = D^v(L_a^v). \tag{4.12}$$

4.3 Forming fabric flow

The flow over three different industrial forming fabrics are investigated through simulation. Triangulations of the three fabrics are shown in Figure 4.3. Fabric A is a double layer fabric used mainly for graphical papers (newsprint, light weight coated paper and supercalendered paper) and for the printing ply on high quality board (liquid packaging board and folding box board). Fabric B is a warp bound triple layer fabric, mainly used on different packaging applications, as on filler plies on multi-ply board machines and on liner and fluting machines. Fabric C is a fine sheet support binder fabric and has similar applications as Fabric A.

The fabrics are positioned in a box-like simulation domain such that the main flow is directed in the negative z-direction. The planar x-y-dimension of the simulation domain is equal to the size of the fabric triangulations, around 3×3 mm^2. Two types of simulations are performed. One type where the flow is accelerated by a prescribed pressure drop between the inlet and outlet, and one type where the inlet velocity is prescribed. The latter setup is similar to the cylinder simulations. For the first setup, the pressure drops are varied and the CFM-values of the air flow are calculated.

For the simulations with fixed inlet velocity, the proposed impact measures are calculated. First the flow is simulated for $Re = 20$, calculated based on the thread diameter of the fabrics. Since the different fabrics have different thread diameters, the mean diameter of the different threads in the top layer is used to calculate the Reynolds numbers. The normalized values of the measures are

(a) Fabric A paper side.   (b) Fabric B paper side.   (c) Fabric C paper side.

(d) Fabric A wear side.   (e) Fabric B wear side.   (f) Fabric C wear side.
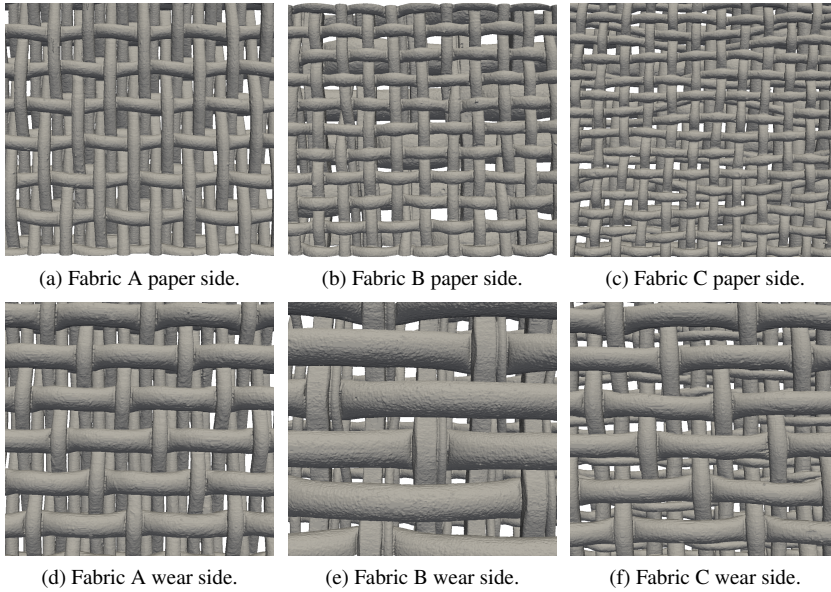
Figure 4.3: Triangulations of the three different industrial forming fabrics studied in this work. The snapshots are from above (paper side) and from below (wear side). The dimension of the snapshots are approximately 3×2.8 mm^2 $(x \times y)$.

compared to the cylinders study. However, to compare the characteristics of the fabrics, also the absolute values of the measures are of interest. For this purpose, additional simulations are used with the same inlet velocity for all three fabric types.

In addition to the CFM-measure and the novel impact measures, the drainage marking of the three fabrics are analysed by examining the flow fields upstream.

4.4   Main results

In this section, a selection of velocity profiles are shown from the simulations of the flow over cylinders. For more velocity profiles, impact measure values, and the other types of plots, see Paper IV. The main conclusions of the cylinder study is presented briefly. Moreover, results from the fabric investigation are described.

In Figure 4.4, the v- and u-velocity profiles for the flow over one cylinder is plotted for $Re = 20$. The profiles are extracted at three different upstream

positions, $y/d = 1$, $y/d = 0.5$, and $y/d = 0.25$. In a similar way, profiles for the flow over one row of cylinders are shown in Figure 4.5. The normalized surface spacings are $g = 0.25, 1, 5, 10$. The dashed lines correspond to profiles for one cylinder. In Figure 4.6, some profiles for the flow over two rows of cylinders are shown.
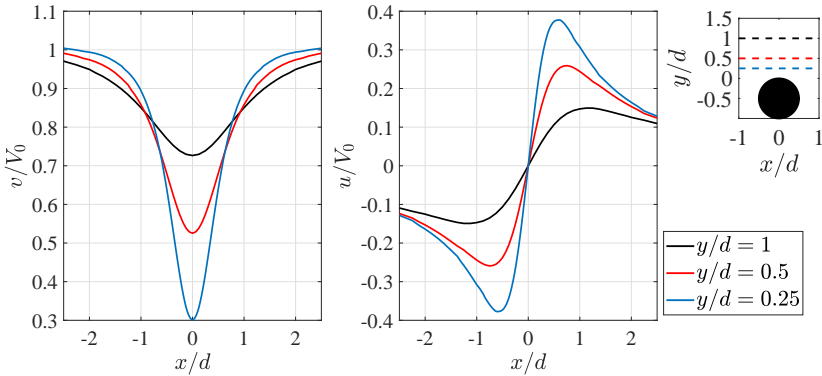

Figure 4.4: The normalized velocity profiles for the flow over one cylinder at $Re = 20$. To the left the v-profile and to the right the u-profile. The profiles are extracted at three positions upstream, $y/d = 1, 0.5, 0.25$.

The Reynolds number dependency on the upstream flow features are investigated by simulating the flow over one cylinder and rows of cylinders, for different Reynolds number in the range $Re \in [1, 80]$. By comparing the resulting velocity profiles, the conclusion is drawn that varying the Reynolds number does not affect the feature of the upstream flow in the investigated range. The profiles have similar shapes and are merely translated upwards when the Reynolds number is increased. Therefore, only the case $Re = 20$ is investigated in detail for different configurations.

There are two main observations regarding the difference between the upstream flow over one or two cylinders and rows of cylinders. The first observation is that when one or two cylinders are considered, the maximum velocity in the domain is never larger than the mainstream velocity except for some few percent. For rows of cylinders, this is not the case and the velocity is considerably higher than the mainstream velocity, with increased values in the regions above the holes in-between the cylinders. The second observation is related to the surface spacing. It is seen that the range of impact is drastically reduced
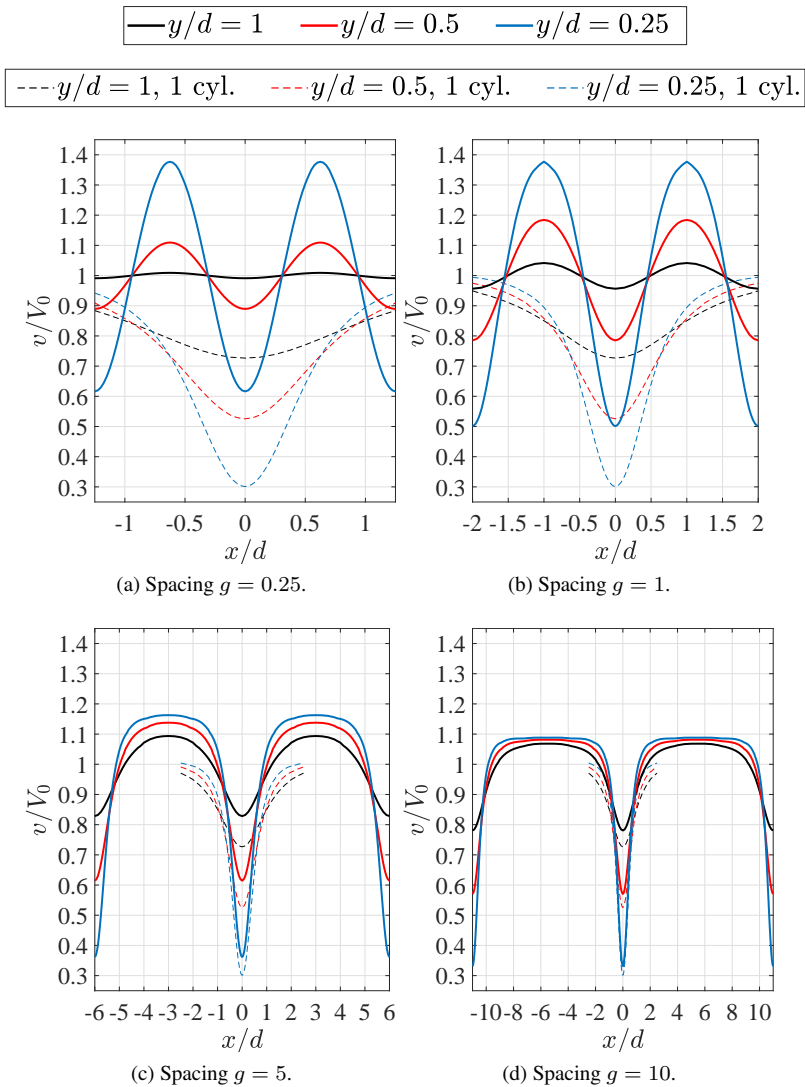
Figure 4.5: The normalized velocity profiles v/V_0 for the flow over one row of cylinders with $Re = 20$ for spacings $g \in \{0.25, 1, 5, 10\}$. The profiles have been plotted at three different positions upstream, $y/d = 1, 0.5, 0.25$. The dashed curves are the profiles for the one-cylinder case.

for rows of cylinders with surface spacing less than one cylinder diameter. At a position $y/d = 1$ upstream, the velocity profiles deviate less than 5 % from the

(a) Spacings $g = 5$ and $l = 0.1$.

(b) Spacings $g = 5$ and $l = 1$.
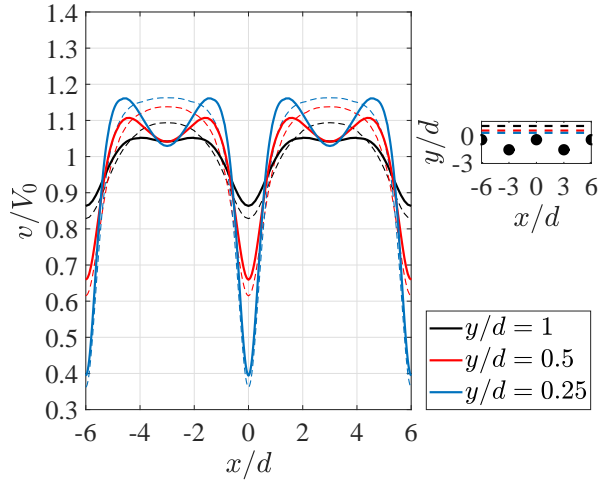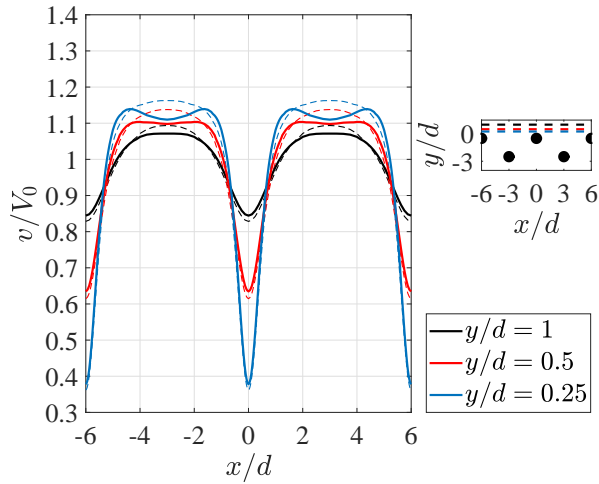
Figure 4.6: The normalized velocity profiles for v/V_0 for the flow over two rows of cylinders where the second row is displaced. Two setups are shown, $g = 5$ and $l \in \{0.1, 1\}$. The dotted lines show the profile for the flow over one row of cylinders.

mainstream velocity.

By comparing the tandem setup with the side-by-side setup for two cylin-

ders, and analogously the tandem with the displaced setup for two rows of cylinders, the same conclusions are drawn. The upstream impact of a tandem cylinder is negligible. This is not the case for the displaced configuration of two rows of cylinders, where the second row influences the upstream flow. The magnitude of this impact increases when the row spacing l decreases. However, for small surface spacings, starting somewhere in $g \in [1,3]$, the effect from the second row is close to negligible, even though the second row is displaced.

The air flow over the three fabrics in Figure 4.3 is simulated and the CFM-values are calculated for different pressure drops. The results are compared with experimental measurements showing excellent agreement. The CFM-values are plotted in Figure 4.7.
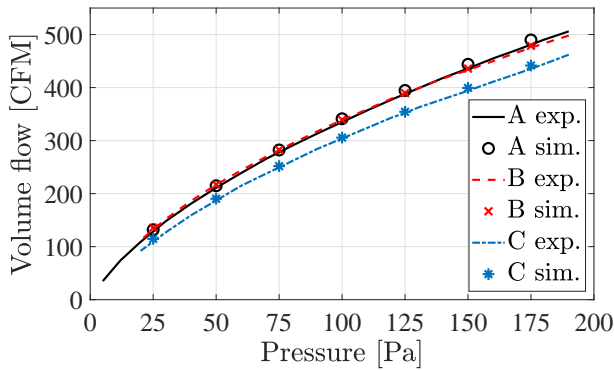
Figure 4.7: Experimental and simulated values of the volume flow of air per area through the three forming fabrics.

By calculating an approximate g-value for the forming fabrics, the results of the cylinder study is compared with the three different fabrics with respect to the g-value dependency. This comparison is performed using the proposed impact measures. It is concluded (see Paper IV for plots) that the same tendencies as for the cylinders hold true for fabrics, that is, for smaller g-values, the upstream range of impact is reduced. Considering the absolute values of the impact measures enables analysis of the relation between the resulting values and the applications of the three different fabrics. Fabric A and C are both used for finer paper while Fabric B is for coarse filler plies in packages. For the length measure, the values are higher for Fabric B compared to the other two fabrics. This trend is not seen by comparing the CFM-values of the three fabrics.

Lastly, drainage marking of the three fabrics are investigated. In Figure 4.9, the upstream velocity field is shown in a x-y-plane at a position $z = 0.15$

mm over the fabric surface. The simulations are performed with a fixed inlet velocity of 2 m/s in the negative z-direction. In Figure 4.8, the velocity profiles of the z-velocities are plotted for the three fabrics. The profiles are extracted at a position $z = 0.15$ mm over the fabric in a line parallel to the x-axis. From both the field and profile plots it is seen that the flow periodicity of Fabric B has larger wave-length compared to the other two fabrics. By inspection of the second layer of Fabric B, it is concluded that the diagonal drainage marking pattern is related to where the large threads in the second layer go up and touch the first layer. This shows that the effect of the second layer is important.
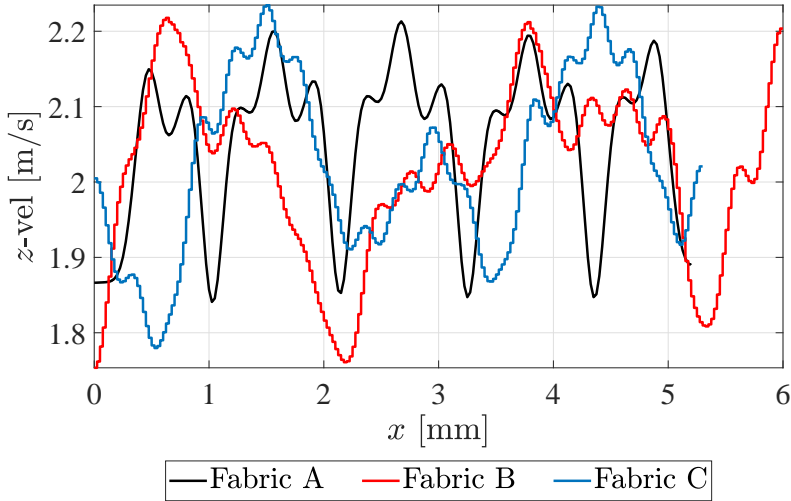
Figure 4.8: Upstream z-velocity profiles extracted in a line parallel to the x-axis at position $z = 0.15$ mm over the fabric surface. Inlet speed is 2 m/s in negative z-direction. In Fig 4.9, it is indicated where in the x-y-plane the profiles are extracted.
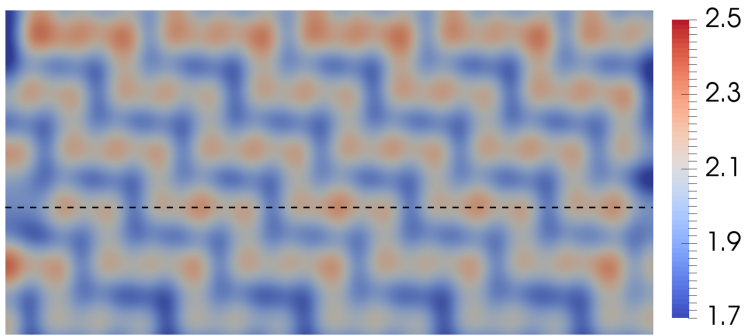
(a) Fabric A
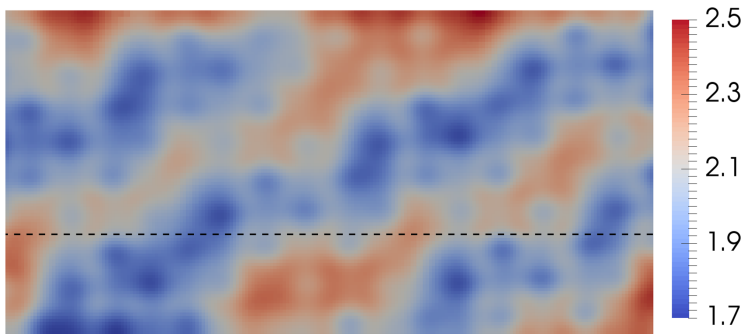
(b) Fabric B
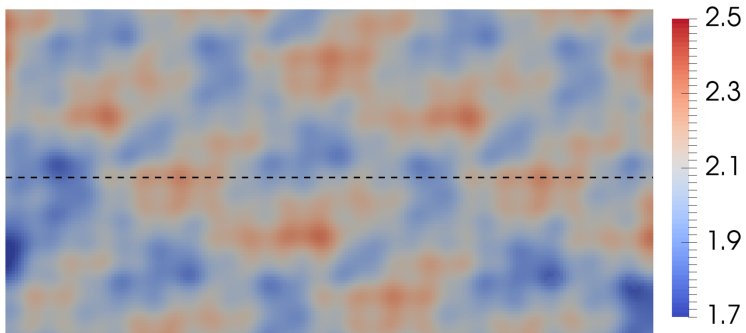
(c) Fabric C

Figure 4.9: Upstream z-velocity field at position $z = 0.15$ mm over the fabric surface. Inlet speed is 2 m/s in negative z-direction. The dimension is 5.2×2.6 mm^2. The black dashed lines indicate where the velocity profiles in Fig 4.8 are extracted.

5. Discrete Fiber Network Model

One aim of developing a simulation framework for paper forming is to be able to simulate the lay down process in a paper machine and attain virtual paper sheets with a realistic structure. With virtual fiber sheets at hand, the next step is to study their mechanical properties, such as the strength and stiffness. The fiber suspension model proposed in this work is constructed to capture the fluid dynamical aspects and interactions occurring during the lay down. For simulation of the mechanical properties of fiber networks, a model with such a detailed description of the fluid dynamics and fiber-fiber interactions is not necessary. Instead a fiber network model is more suitable.

In this chapter, a discrete fiber network model is presented. The model is elementary and serves as a starting point for capturing the mechanical properties of the virtual fiber networks attained from the lay down simulations, as well as an instrument for the development of the numerical multiscale method presented in the next chapter. The network model is inspired by mass-spring models [49], where a network is defined as built up of edges and nodes and where each edge has the mechanical properties of a spring. The network model presented in this work has two features in addition to the basic spring property resisting extension of edges. First, a spring-like resistance to angular change between pair of edges is included. Secondly, a novel effect in the form of a resistance to changes in the total length of pairs of edges, resulting in a response similar to the Poisson effect.

In Section 5.1, the overall idea of a network model is explained. Thereafter,

notations and definitions for the proposed network model is given in Section 5.2. In Sections 5.3-5.5, the three force contributions of the model is presented. In Section 5.6, it is explained how the governing equations are assembled. Lastly, the relation to the linear elasticity equation is shown.

5.1   Overall idea

The overall idea of a network model is to represent a material as a structure consisting of elements with properties such that the structure as a whole represents the properties of the material. If such a model fulfils its purposes, it can be used to simulate additional properties of the material. The network model developed in this work is very simple in regard to structure, only consisting of edges and nodes. For a fiber network (see Figure 1.4), which is the material of interest in this context, each fiber can be built up of a chain of edges. The fibers can in turn be bonded together by, in the simplest case, letting nodes of different fibers be kept together, or using a more advanced setup, connecting two fibers with a structure of edges, giving the bond certain desired properties. In a more general perspective, the network model could equally well represent a discretization of a solid object, such as for example a concrete structure. It will be shown that the network model proposed in this work, for certain choices of parameters, is equivalent to the finite difference discretization of the linear elasticity equation.

Consider a network consisting of edges and nodes. In this work, the governing equations are derived from force equilibrium equations assembled at each node. By considering edges and pair of edges, and defining what forces that acts on the nodes when they are displaced, the equations are attained. In this model, three types of force contributions are included. First, considering a single edge, a spring force is defined acting to restore changes in length that occurs when the nodes of the edge are displaced. Second, considering a pair of two edges connected at a common node, an angular spring force is defined which acts to restore changes in the angle between the two edges by applying a torque at the common node, a torque which is transformed to a force couple. Third, again considering a pair of edges, a force contribution is defined which acts to restore the total length of the two edges of the pair, giving an effect similar to the Poisson effect.

The network model presented in this chapter is two-dimensional, static and assumes small deformations.

5.2   Notations and definitions

Consider a two-dimensional network $(\mathcal{N}, \mathcal{E}, \mathcal{P})$, where $\mathcal{N}$ is the set of node indices, $\mathcal{E}$ is the set of edges, and $\mathcal{P}$ is the set of edge pairs. A node $i \in \mathcal{N}$ is defined by its initial position $p_i \in \mathbb{R}^2$, and its displacement $\delta_i \in \mathbb{R}^2$. In Figure 5.1, the notations are illustrated. Let the total number of nodes be denoted N.

(a)

(b)
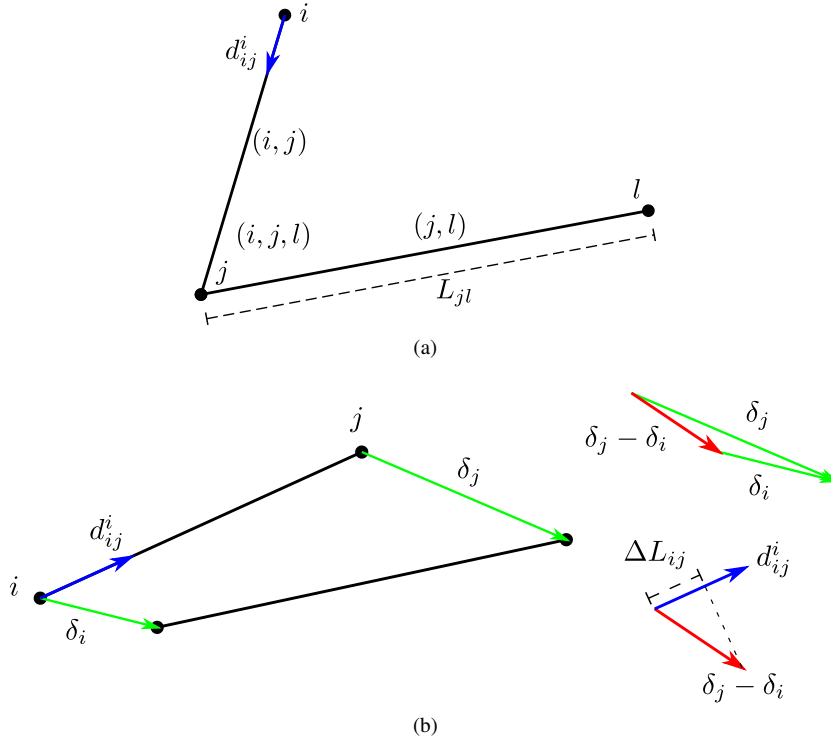
Figure 5.1: Sketches showing the notation used for the network nodes, edges and edge pairs. In the upper sketch, three nodes are shown, connected as two edges, which in turn are connected as an edge pair. In the lower sketch, the approximate length change ΔL_{ij} of an edge (i, j) is illustrated.

An edge $(i, j) \in \mathcal{E}$ is defined as the connection between the two nodes i and j. It is assumed that (i, j) and (j, i) define the same edge. The direction vector of edge (i, j) with respect to node $a \in \{i, j\}$ is defined as (see Figure 5.1)

$$d_{ij}^a = \frac{p_b - p_a}{|p_b - p_a|}, \quad b \in \{i, j\},\ b \neq a. \tag{5.1}$$

Let L_{ij} denote the initial length and w_{ij} the initial width of edge (i, j), where the width is uniform across the whole edge. The out-of-plane thickness of the edges are assumed to be constant equal to z. The length change ΔL_{ij} of edge (i, j) is defined as the projection of the difference between the displacement of the nodes onto the direction vector, i.e.

$$\Delta L_{ij} = (\delta_j - \delta_i) \cdot d_{ij}^i. \tag{5.2}$$

In Figure 5.1b, the length change ΔL_{ij} is illustrated. The mechanical properties of edge (i, j) is defined by the stiffness parameter k_{ij}.

An edge pair $(i, j, l) \in \mathcal{P}$ is defined as two edges, (i, j) and (j, l), connected at node j (see Figure 5.1a). Note that (i, j, l) and (l, j, i) define the same edge pair. The mechanical properties of an edge pair are defined by the parameter κ_{ijl}, describing the resistance to angular change between the two edges. The joint volume at the mutual node j is denoted V_{ijl}. The parameters η_{ijl} and γ_{ijl} define the Poisson effect described in Section 5.5.

5.3   Edge extension

The first force contribution acts at edges, giving a resistance to changes in the length of the edge. Consider an edge $(i, j) \in \mathcal{E}$. When the nodes of the edge are displaced such that the length change ΔL_{ij} is non-zero, two anti-parallel forces are set to act at the nodes of the edge to restore the length change to zero. The forces are calculated according to a classic spring force relation:

$$F_a^{\mathrm{I}}(i, j) = k_{ij} \frac{w_{ij} z}{L_{ij}} \Delta L_{ij} d_{ij}^a, \quad a \in \{i, j\}. \tag{5.3}$$

The direction of the forces are parallel to the initial direction of the edge. In Figure 5.2, the edge extension forces are illustrated for the cases of positive and negative length change.

5.4   Angular deviation

The second force contribution acts at edge pairs by introducing a resistance to changes in the angle between the two edges. Consider an edge pair $(i, j, l) \in \mathcal{P}$. When the angle between the two edges changes, two opposite torques are applied at the mutual node, acting on one edge each. These torques are calculated similarly as for a spring condition. The two torques are transformed into force couples and the resulting forces are applied to the nodes of the edge pair. In Figure 5.3, the resulting forces are illustrated for the two cases of increased and
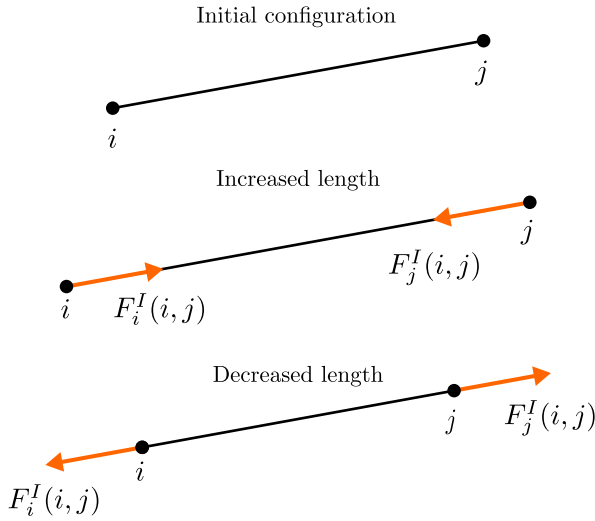
Figure 5.2: At the top, an edge (i, j) is shown in its initial configuration. Below the forces that act on the nodes when they are displaced are shown both for the case of increased and decreased length.

decreased angle between the edges.

To calculate the angle changes of the edges, edge normals, n_{ji}^j and n_{jl}^j (see Figure 5.3), are defined according to

$$
\begin{aligned}
n_{ji}^j &= d_{ji}^j \times \hat{z}, \\
n_{jl}^j &= -d_{jl}^j \times \hat{z}.
\end{aligned}
\tag{5.4}
$$

By assuming small angular changes and using the approximation $\alpha \approx \tan \alpha$, the angle changes of the two edges, $\delta\theta_{ji}$ and $\delta\theta_{jl}$ (see Figure 5.3), are calculated as

$$
\delta\theta_{ja} \approx \tan \delta\theta_{ja} = \frac{(\delta_a - \delta_j) \cdot n_{ja}^j}{L_{ja}}, \quad a \in \{i, l\}.
\tag{5.5}
$$

The total angle change of the edge pair, $\Delta\theta_{ijl}$, is calculated as the sum of the two separate angle changes $\delta\theta_{ja}$, $a \in \{i, l\}$,

$$
\Delta\theta_{ijl} = \delta\theta_{ji} + \delta\theta_{jl}.
\tag{5.6}
$$
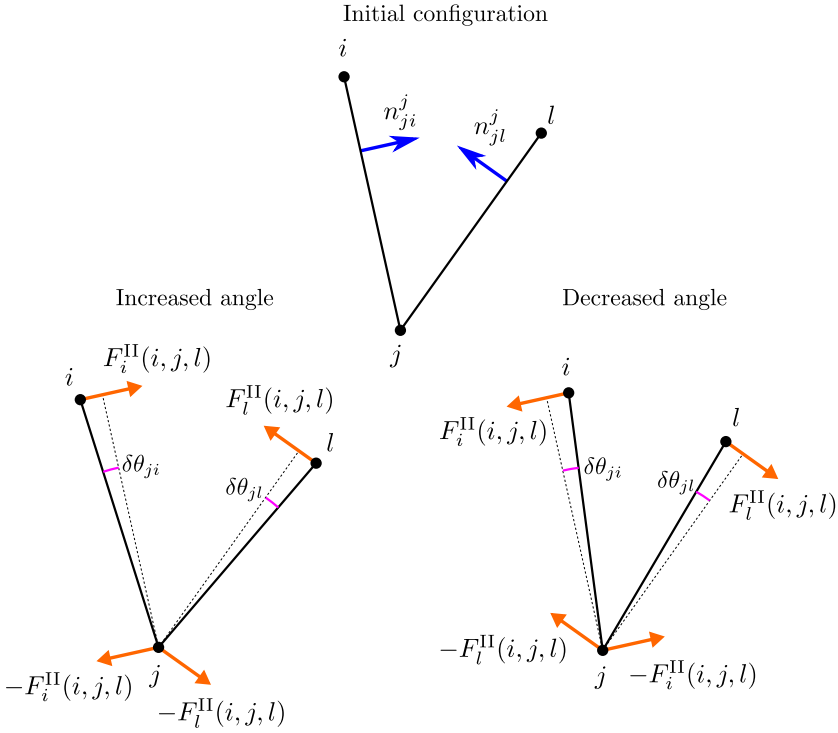
Figure 5.3: Illustration of an edge pair and the forces that acts on the nodes when the angle between the edges is increased or decreased. Uppermost, the edge pair in its initial configuration is shown. The edge normals n_{ji}^j and n_{jl}^j are depicted. Below to the left, the case of increased angle is shown, and to the right the case of decreased angle. The dashed lines indicate the initial configuration of the edges.

The two torques acting on edge (i, j) and (l, j) at node j are given by

$$\tau_i = \kappa_{ijl} V_{ijl} \Delta\theta_{ijl} \hat{z},$$
$$\tau_l = -\tau_i.$$

The bending parameter κ_{ijl} and the joint volume V_{ijl} lead to higher resistance to bending when the values are increased. Transforming the two torques into

two force couples results in

$$F_a^{\mathrm{II}}(i,j,l) = -\frac{\kappa_{ijl} V_{ijl} \Delta\theta_{ijl}}{L_{aj}} n_{ja}^j, \quad a \in \{i,l\},$$

$$F_j^{\mathrm{II}}(i,j,l) = -F_i^{\mathrm{II}}(i,j,l) - F_l^{\mathrm{II}}(i,j,l).$$

5.5 Poisson effect

The third force contribution acts on edge pairs. It adds a resistance to changes in the total length of the two edges of the pair. Consider an edge pair $(i,j,l) \in \mathcal{P}$. When edge (j,l) changes length, it is assumed that its width changes according to the Poisson effect described by the parameter γ_{ijl}. This change in width of edge (j,l) creates a tension in the other edge in the pair so that forces start to act at the two nodes of the other edge. In Figure 5.4, this phenomenon is illustrated. The magnitude of these two forces is given by a spring expression depending on the difference between the length change, ΔL_{ij}, of edge (i,j), and the width change attained from the Poisson effect. The analogous reasoning applies for a width change of the other edge. The resulting forces acting at the outer nodes $a \in \{i,l\}$ will be

$$F_a^{\mathrm{III}}(i,j,l) = -\eta_{ijl} \frac{w_{aj}z}{L_{aj}} \left(\Delta L_{aj} + \gamma_{ijl} \frac{w_{bj}}{2} \frac{\Delta L_{bj}}{L_{bj}} |n_{aj}^j \cdot d_{bj}^j| \right) d_{aj}^j,$$

$$a,b \in \{i,l\}, \ b \neq a,$$

and at the central node:

$$F_j^{\mathrm{III}}(i,j,l) = -F_i^{\mathrm{III}}(i,j,l) - F_l^{\mathrm{III}}(i,j,l).$$

5.6 Assembly of the global governing equation

The global matrix system governing the displacements of the network nodes is attained by assembly of the equilibrium equations for all nodes. Each edge and each edge pair contribute with their own element matrix and all these separate matrices sum up to the global elasticity matrix.

Let $u \in \mathbb{R}^{2N}$ denote the solution vector containing all node displacements according to the division

$$\begin{bmatrix} u(2i-1) \\ u(2i) \end{bmatrix} = \delta_i, \quad 1 \leq i \leq N.$$

Initial configuration
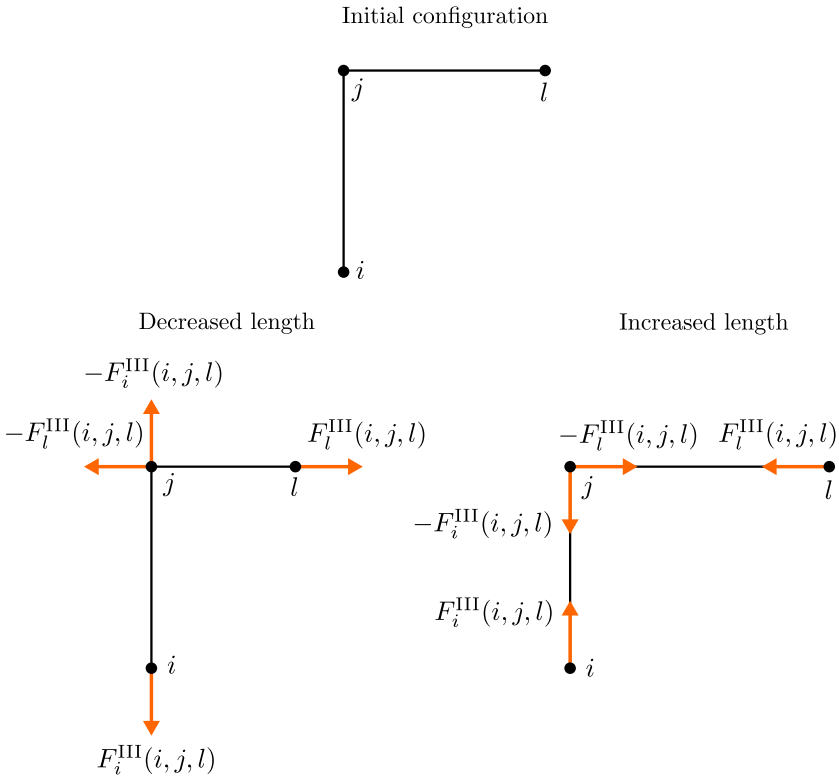
Figure 5.4: Illustration of the force contribution which gives an effect similar to the Poisson effect. Uppermost, an edge pair (i, j, l) in its initial configuration is shown. Below, two cases are depicted. One where the upper edge decreases in length and one where the upper edge increases in length. The resulting forces acting on the nodes are shown for the two cases.

Similarly, let $F \in \mathbb{R}^{2N}$ denote the load vector with forces applied to the nodes. The governing equation of the network reads

$$Ku = F, \tag{5.7}$$

where $K \in \mathbb{R}^{2N \times 2N}$ is the elasticity matrix. Next, it is described how the matrix is assembled.

As stated above, for each edge and edge pair, the three force contributions can be calculated separately and assembled into separate matrices which are added together to attain the global elasticity matrix. Let $K_{ij}^{\mathrm{I}}, K_{ijl}^{\mathrm{II}}, K_{ijl}^{\mathrm{III}} \in$

$\mathbb{R}^{2N \times 2N}$ denote the matrices assembled from the first, second and third force contribution respectively, at different elements (edges (i,j) or edge pairs (i,j,l)). These matrices are sparse and the only non-zero elements are defined by the relations

$$
\begin{aligned}
K_{ij}^{\mathrm{I}}(\{2a-1, 2a\}, \{1, \dots, 2N\})u &= F_a^{\mathrm{I}}(i,j), & a &\in \{i,j\}, \\
K_{ijl}^{\mathrm{II}}(\{2a-1, 2a\}, \{1, \dots, 2N\})u &= F_a^{\mathrm{II}}(i,j,l), & a &\in \{i,j,l\}, \\
K_{ijl}^{\mathrm{III}}(\{2a-1, 2a\}, \{1, \dots, 2N\})u &= F_a^{\mathrm{III}}(i,j,l), & a &\in \{i,j,l\}.
\end{aligned}
$$

The elasticity matrix K is assembled according to

$$
K = - \sum_{(i,j) \in \mathcal{E}} K_{ij}^{\mathrm{I}} - \sum_{(i,j,l) \in \mathcal{P}} \left(K_{ijl}^{\mathrm{II}} + K_{ijl}^{\mathrm{III}} \right).
$$

The resulting elasticity matrix is symmetric and positive semi-definite.

5.7   Relation to linear elasticity theory

The network model presented in this chapter is under certain conditions equivalent to the finite difference discretization of the linear elasticity equation.

The two-dimensional elasticity equations reads

$$
\begin{aligned}
\mu \nabla^2 u + (\lambda + \mu) \frac{\partial}{\partial x} \left(\frac{\partial u}{\partial x} + \frac{\partial v}{\partial y} \right) + f_x &= 0, \\
\mu \nabla^2 v + (\lambda + \mu) \frac{\partial}{\partial y} \left(\frac{\partial u}{\partial x} + \frac{\partial v}{\partial y} \right) + f_y &= 0,
\end{aligned}
\tag{5.8}
$$

where μ and λ are the Lame's parameters, and f_x and f_y are the applied force densities in the x- and y-direction, respectively. In the equations, u and v denote the x- and y-displacements.

Consider a network with rectangular pattern as depicted in Figure 5.5. Each node is the central node in four edge pairs and the outer node in eight edge pairs. Parallel edges are not considered in an edge pair even though they have a node in common. Let the edge length be $L_{ij} = h$ and the edge width $w_{ij} = w = ch$, where c is a constant. Assume that all parameters are uniform over the network such that $k_{ij} = k$, $\kappa_{ijl} = \kappa$, $\gamma_{ijl} = \gamma$ and $\eta_{ijl} = k$. Moreover let the joint volume of the edge pairs be $V_{ijl} = c^2 h^2$.
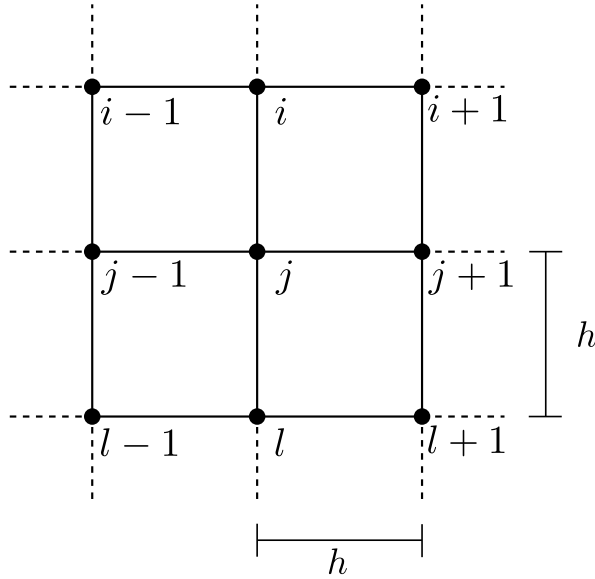
Figure 5.5: Part of a network with uniform rectangular pattern. Nine nodes and twelve edges are depicted. The edge length $L_{ij} = h$ is illustrated.

Theorem 1. *Consider a network with rectangular pattern and uniform coefficients as described above. If the parameters are given as*

$$
\kappa = \frac{\mu}{4c^2},
$$
$$
\gamma = \frac{\lambda}{2c^2\eta}, \tag{5.9}
$$
$$
k = \frac{\lambda + 2\mu}{c} - 4\eta,
$$

then the governing equation of the network is equivalent to the finite difference discretization of the elasticity equation (5.8) with Lame's parameters μ and λ.

Proof. Consider node j in Figure 5.5. We construct its force equilibrium equation by using the network model and compare the results to the finite difference discretization of the elasticity equation (5.8). The force equilibrium equation

for node j is

$$\sum_{(a,b)\in\mathcal{E}_j} F_j^{\mathrm{I}}(a,b) + \sum_{(a,b,c)\in\mathcal{P}_j} F_j^{\mathrm{II}}(a,b,c) + \sum_{(a,b,c)\in\mathcal{P}_j} F_j^{\mathrm{III}}(a,b,c) + F^{\mathrm{Ext}} = 0,$$

(5.10)

where

$$\mathcal{E}_j = \{(j,j-1),\,(j,j+1),\,(j,i),\,(j,l)\}$$

(5.11)

is the set of edges connected to node j, and

$$\begin{aligned}\mathcal{P}_j = \big\{&(i,j,j+1),\,(i,j,j-1),\,(l,j,j+1),\,(l,j,j-1),\\&(j,i,i-1),\,(j,i,i+1),\,(j,j-1,i-1),\,(j,j+1,i+1),\\&(j,j-1,l-1),\,(j,j+1,l+1),\,(j,l,l-1),\,(j,l,l+1)\big\}\end{aligned}$$

(5.12)

is the set of all edge pairs containing j. It is assumed that the external force can be written as

$$F^{\mathrm{Ext}} = \begin{bmatrix} h^2 z f_x \\ h^2 z f_y \end{bmatrix}.$$

(5.13)

Since the edges of the network is parallel to the x- or y-axis the direction and normal vectors are simple and the equilibrium equation can be considerably simplified. The sum of the first force contribution is simplified to

$$\sum_{(a,b)\in\mathcal{E}_j} F_j^{\mathrm{I}}(a,b) = kcz \begin{bmatrix} u_{j-1} - 2u_j + u_{j+1} \\ v_i - 2v_j + v_l \end{bmatrix}.$$

(5.14)

The sum of the second force contribution is simplified to

$$\begin{aligned}&\sum_{(a,b,c)\in\mathcal{P}_j} F_j^{\mathrm{II}}(a,b,c) =\\&\kappa c^2 z \begin{bmatrix} 4\left(u_i - 2u_j + u_l\right) + v_{l-1} - v_{i-1} + v_{i+1} - v_{l+1} \\ 4\left(v_{j-1} - 2v_j - v_{j+1}\right) + u_{l-1} - u_{i-1} + u_{i+1} - u_{l+1} \end{bmatrix}.\end{aligned}$$

(5.15)

The sum of the third force contribution is simplified to

$$
\sum_{(a,b,c)\in\mathcal{P}_j} F_j^{\mathrm{III}}(a,b,c) =
$$

$$
\eta c z \left[\begin{array}{l} 4\left(u_{j-1} - 2u_j + u_{j+1}\right) + \frac{\gamma c}{2}\left(v_{l-1} - v_{i-1} + v_{i+1} - v_{l+1}\right) \\ 4\left(v_l - 2v_j - v_i\right) + \frac{\gamma c}{2}\left(u_{l-1} - u_{i-1} + u_{i+1} - u_{l+1}\right) \end{array} \right].
$$

$$(5.16)$$

Inserting the derived expressions into the equilibrium equation (5.10), and dividing by $h^2 z$ gives the system

$$
c(k+4\eta)\frac{u_{j-1} - 2u_j + u_{j+1}}{h^2} + 4\kappa c^2 \frac{u_i - 2u_j + u_l}{h^2}
$$
$$
+2c^2\left(2\kappa + \eta\gamma\right)\frac{v_{l-1} - v_{i-1} + v_{i+1} - v_{l+1}}{4h^2} + f_x = 0,
$$
$$
c(k+4\eta)\frac{v_i - 2v_j + v_l}{h^2} + 4\kappa c^2 \frac{v_{j-1} - 2v_j - v_{j+1}}{h^2}
$$
$$
+2c^2\left(2\kappa + \eta\gamma\right)\frac{u_{l-1} - u_{i-1} + u_{i+1} - u_{l+1}}{4h^2} + f_y = 0.
$$

$$(5.17)$$

It can be seen that the second order finite differences of the second order standard and mixed derivates are present in the equation system above. Let $h \to 0$, and compare the system with the linear elasticity equations (5.8). By matching the coefficients in front of the different derivatives the following must hold

$$
\lambda + \mu = 2c^2\left(2\kappa + \eta\gamma\right),
$$
$$
\mu = 4\kappa c^2,
$$
$$
\lambda + 2\mu = c\left(k + 4\eta\right).
$$

$$(5.18)$$

These relations are equivalent to what was given in the statement of the theorem.

□

Additionally, it can be noted that for a straight line parallel to the x-axis, divided into a number edges with equal length, two well-known finite difference stencils emerge from the different force contributions of the network model. For the edge extension forces, described in Section 5.3, the result is the second order accurate stencil for the second order derivate $\frac{\partial^2 u}{\partial x^2}$, that is $1, -2, \ 1$. For the angular deviation forces, described in Section 5.4, the result is the second order accurate stencil for the fourth order derivative $\frac{\partial^4 v}{\partial x^4}$ (recall the static Euler-Bernoulli beam equation [17]), that is $1, -4, \ 6, -4, \ 1$.

6. A Multiscale Method for Discrete Network Models

Paper is a complex material whose macroscale properties depend on the microscale structure, which consists of fibers and particles bonded together. The material composition makes network modelling a convenient technique for studying the mechanical properties. However, the multiscale nature of paper makes it challenging to simulate macroscale properties while including the microscale features. To overcome such computational challenges, multiscale methods are a promising approach. In this chapter, a multiscale method for discrete network models, such as the fiber network model described in Chapter 5, is presented.

The multiscale method is based on the Localized orthogonal decomposition method (LOD) [24,46], which is a generalized finite element multiscale method for elliptic partial differential equations with highly varying coefficients. In this work, the LOD method is modified and extended to discrete network models. The idea is to construct a low-dimensional solution space with good approximation properties. This is achieved by defining a symmetric and coercive bilinear operator using the connectivity matrix of the fiber network, and using this operator to form an orthogonal complement of the fine scale space. A basis for the resulting multiscale space is attained by modifying the basis functions of a coarse solution space, which is spanned by a classical finite element basis, for example bilinear shape functions. The basis functions are modified by solving sub-problems. By utilizing the exponential decay of the modifications, the sub-problems can be localized. In this way, the problem size is reduced. Moreover, the setup of the method facilitates parallelization and for simulations of frac-

ture propagation, only the local sub-problems close to broken edges have to be resolved.

In Section 6.1, an overview of the method is presented. In Section 6.2, it is explained how the network is represented geometrically by a coarse grid. Thereafter, the definitions of the coarse space, the detail space and the multiscale space are given in Sections 6.3-6.4. In Section 6.5, the localization is explained. Lastly, in Section 6.6, some error analysis and numerical results are given. For more details, see Paper V.

6.1   Overview of method

Consider a material modelled as a network, whose properties are described by a connectivity matrix $K \in \mathbb{R}^{n \times n}$, where n is the number of degrees of freedom. The typical example in this work is a fiber network of a paper-based material, see Figure 1.4. Suppose that the displacements of the nodes are sought and denote the solution vector $u \in \mathbb{R}^n$. Assume that applied load forces are contained in the vector $F \in \mathbb{R}^n$. To attain a solvable problem, some degrees of freedom have to be constrained, resulting in a governing equation

$$\check{K}u = \check{F}, \tag{6.1}$$

where $\check{K}$ and $\check{F}$ are the modifications of the connectivity matrix and the load vector by explicitly including the constrained degrees of freedom.

The multiscale method presented in this work is developed to solve problems of the form described above. The governing equation (6.1), is reformulated on variational form:

$$\text{Find } u \in V : \quad v^T K u = v^T F, \quad \forall v \in V. \tag{6.2}$$

The solution space $V \subset \mathbb{R}^n$ is attained after constraining some degrees of freedom. The idea is to construct an approximate solution space V_{ms}, which is low-dimensional in comparison to V, and such that the solution of the multiscale problem

$$\text{Find } u_{\text{ms}} \in V_{\text{ms}} : \quad v^T K u_{\text{ms}} = v^T F, \quad \forall v \in V_{\text{ms}}, \tag{6.3}$$

results in a small error $\|u - u_{\text{ms}}\|$ in some preferred norm.

To construct the multiscale space, first the network is covered by a grid. A coarse space is defined as the span of shape functions defined over the grid as in the finite element method. In this work, the space is chosen as the span of

classic bilinear basis functions. A detail space is defined such that the coarse space and the detail space constitute a splitting of the solution space V. This detail space is used to define the multiscale space by using the K-matrix as a bilinear form $v^T K w$, which works if K is symmetric and positive definite in the space V. The multiscale space is defined as the K-orthogonal complement of the detail space.

To solve the multiscale problem (6.3), a basis is constructed which is used to convert the variational formulation (6.3) into a simple matrix equation similarly as in the finite element method. The multiscale basis is attained by solving sub-problems resulting in corrections, used to modify the bilinear basis. The global multiscale system (6.3) will be small in size while the local sub-problems will have the same size as the original system (6.1). However, from numerical investigation, it is seen that the corrections decrease exponentially, which is also proved theoretically for the original LOD method [24]. Due to the exponential decay, the sub-problems can be localized, resulting in problems of much smaller size. In this way the maximum size of any problem that has to be solved is reduced considerably compared to the size of the original problem (6.1). Moreover, if fracture propagation is simulated, the proposed method has the feature that only basis functions close to the resulting fracture have to be recomputed. The method also facilitates parallelization, by solving the sub-problems in parallel, and if different load vectors F are considered, only the final low-dimensional multiscale problem (6.3) has to be recomputed for each new load vector.

6.2 Coarse grid representation

Let the network be represented by a coarse grid covering the network geometry. The coarse grid can for example be a triangulation or a quadrilateration of the computational domain covering the network. In Figure 6.1a, an illustration of a network and its coarse grid representation are shown. The coarse grid should constitute a good approximation of the computational domain of the network, and in this work, networks of rectangular shape are considered which correspond well to the problem of investigation of paper sheets. The degrees of freedom of the coarse grid nodes correspond to the dimension of the multiscale solution space, and the solution of the multiscale problem will be the displacements of the coarse nodes.

Let m be the number of degrees of freedom of the coarse nodes. Some coarse degrees of freedom are constrained, resulting in m_H active degrees of freedom, which correspond to the dimension of the coarse solution space de-

(a) Network and FEM quadrilateration.   (b) A bilinear basis function $\Lambda_i : \mathbb{R}^2 \to \mathbb{R}$ of the
                                          FEM grid.
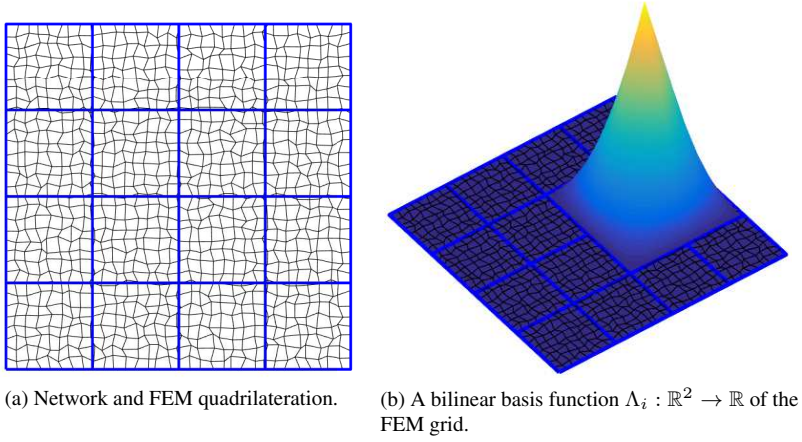
Figure 6.1: Example of a square network with randomly perturbed interior
nodes, represented with a coarse FEM quadrilateration and bilinear basis func-
tions.

fined in the next section. Let $\mathcal{M} \subset \{1, \ldots, m\}$ be the set of indices of the
active coarse degrees of freedom.

   In this work, a quadrilateration is used as the coarse grid. Let $\Lambda_i : \mathbb{R}^2 \to$
$\mathbb{R}, i = 1, \ldots, m$ be bilinear basis functions defined over the coarse grid sim-
ilarly as in the finite element method. Hence, by a linear combination of the
basis functions weighted with the displacements of each coarse degree of free-
dom, the displacement of any point in the support of the coarse grid can be
calculated, and in this way all network nodes are given a displacement from the
coarse representation. In Figure 6.1b, an example of a bilinear basis function
for a coarse grid representation is illustrated.

6.3   Coarse space and detail space

The coarse space, V_H, is defined as a subspace of V by using the bilinear basis
functions. Let $\lambda_i \in \mathbb{R}^n, i = 1, \ldots, m$ be the interpolation of the bilinear basis
functions Λ_i to the network nodes according to

$$\lambda_i(j) = \begin{cases} \Lambda_i(p_j), & \text{if} \quad i \equiv j \pmod{d}, \\ 0, & \text{else}, \end{cases} \qquad (6.4)$$

where d is the dimension of the space the network resides in and $p_j \in \mathbb{R}^d$ is the position of the node corresponding to degree of freedom j. The coarse space $V_H \subset V$ is defined as the span of the interpolated basis vectors which correspond to active coarse degrees of freedom, that is

$$V_H = \text{span}(\{\lambda_i\}_{i \in \mathcal{M}}). \tag{6.5}$$

By introducing the matrix $B_H = [\{\lambda_i\}_{i \in \mathcal{M}}] \in \mathbb{R}^{n \times m_H}$, having the interpolated basis vectors corresponding to the active coarse degree of freedoms as its columns, an equivalent definition of the coarse space is

$$V_H = \{B_H B_H^T v : v \in V\}. \tag{6.6}$$

The matrix B_H is called the prolongation matrix.

The coarse space is defined as the range of the prolongation matrix, while the detail space, W, is defined as the kernel of a restriction matrix $C_H \in \mathbb{R}^{m_H \times n}$. In this work, the restriction matrix is chosen as $C_H = B_H^T$, see [23] for different choices of restriction operator for the LOD method. The definition of the detail space reads

$$W = \{v \in V : C_H v = 0\}. \tag{6.7}$$

The coarse space and the detail space constitute a splitting of the solution space V such that any $v \in V$ can be decomposed as $v = v_H + w$, where $v_H \in V_H$ and $w \in W$.

6.4 Multiscale space and multiscale problem

The low-dimensional multiscale space is constructed using the detail space and the connectivity matrix. The multiscale space V_{ms} is defined as the K-orthogonal complement of the detail space W, i.e.

$$V_{\text{ms}} = \{v \in V : w^T K v = 0, \quad \forall w \in W\}. \tag{6.8}$$

Likewise as the coarse space together with the detail space constitute a splitting of V, the multiscale space and the detail space also split V such that any $v \in V$ can be decomposed as $v = v_{\text{ms}} + w$, where $v_{\text{ms}} \in V_{\text{ms}}$ and $w \in W$.

The multiscale solution $u_{\text{ms}} \in V_{\text{ms}}$, to the displacement problem (6.2), is the

solution to the problem

$$\text{Find } u_{\mathrm{ms}} \in V_{\mathrm{ms}} : \quad v^T K u_{\mathrm{ms}} = v^T F, \qquad \forall v \in V_{\mathrm{ms}}. \tag{6.9}$$

To solve the multiscale problem, a basis for the multiscale space V_{ms} is constructed by modifying the basis functions for the coarse space. For each basis function $\lambda_i, i \in \mathcal{M}$, a correction is found as the solution to the problem

$$\text{Find} \quad \phi_i \in W : \quad w^T K (\lambda_i - \phi_i) = 0, \quad \forall w \in W. \tag{6.10}$$

The resulting modified basis $\{\lambda_i - \phi_i\}_{i \in \mathcal{M}}$ constitutes a basis for the multiscale space V_{ms}. In Figure 6.2, the correction ϕ_i and the resulting modified basis $\lambda_i - \phi_i$ are illustrated by an example for a square network with randomly perturbed nodes. For the coarse node at the center of the network, the correction ϕ_i for the x-component is plotted in Figure 6.2a. By subtracting the correction from the original bilinear basis function, the resulting modified basis function $\lambda_i - \phi_i$ is attained, which is plotted in Figure 6.2b.

(a) Correction ϕ_i.   (b) Modified basis function $\lambda_i - \phi_i$.
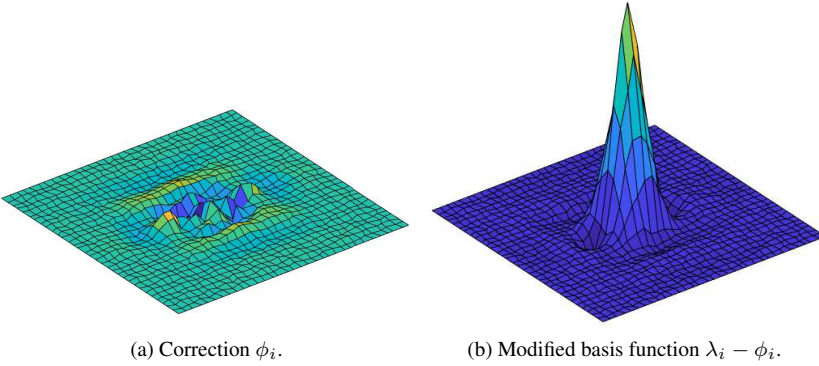
Figure 6.2: The correction ϕ_i and the modified basis $\lambda_i - \phi_i$ for the x-component at the central node of a square network with randomly perturbed interior nodes.

6.5   Localization

Due to the low dimension of the multiscale space V_{ms}, the multiscale problem (6.9) has small size. The correction problems (6.10), which are solved for each basis function corresponding to an active degree of freedom of the coarse grid, have the same size as the original displacement problem (6.2). However, as

is shown numerically in Paper V, the corrections ϕ_i decay exponentially away from their basis nodes [46]. Therefore, the correction problems can be localized by only solving each problem on a restricted domain surrounding its basis node. In this way, the size of the correction problems is reduced. The restricted domains are called patches, and the size can be chosen as a certain layer of coarse grid elements surrounding the considered node. Another choice is to take the patch as a circle with center in the node and with radius ρH, where H is the size of the grid elements, and ρ is the patch size parameter.

6.6   Error analysis

In this section, a summary of the theoretical and numerical analysis of the error of the proposed upscaling method is presented. For a thorough presentation with proofs, see Paper V.

Consider the following three problems:

$$\text{Find } u \in V \quad : \qquad v^T K u = v^T F, \qquad \forall v \in V, \qquad (6.11)$$

$$\text{Find } u_{\text{ms}} \in V_{\text{ms}} : \quad v^T K u_{\text{ms}} = v^T F, \qquad \forall v \in V_{\text{ms}}, \qquad (6.12)$$

$$\text{Find } \tilde{u}_{\text{ms}} \in \tilde{V}_{\text{ms}} : \quad v^T K \tilde{u}_{\text{ms}} = v^T F, \qquad \forall v \in \tilde{V}_{\text{ms}}. \qquad (6.13)$$

The first problem, (6.11), is the original displacement problem with exact solution u. The second problem, (6.12), is the corresponding multiscale problem, and the third problem, (6.13), is the multiscale problem with localized solution space $\tilde{V}_{\text{ms}}$.

First, the difference between the exact solution u and the multiscale solution u_{ms} is analysed.

Proposition 1. *Let $u_f \in W$ be such that $w^T K u_f = w^T F$, $\forall w \in W$. Then the sum $u = u_{\text{ms}} + u_f$, where u_{ms} is the solution to the multiscale problem* (6.12)*, solves the original problem* (6.11)*.*

The proposition shows that the multiscale error, i.e. the difference $u - u_{\text{ms}}$, is in the detail space. If the load vector F is in the coarse space V_H, the error is zero which the following proposition stipulates.

Proposition 2. *Let u and u_{ms} be the solutions to* (6.11) *and* (6.12)*, respectively. If $F \in V_H$, then it holds that $u = u_{\text{ms}}$.*

To analyse the magnitude of the error of the multiscale solution, some as-

sumptions are needed. First two norms and an interpolant are introduced:

$$\|v\| := (v^T K v)^{1/2}, \tag{6.14}$$

$$\|v\|_h := \left(\sum_i \bar{h}_i^2 v_i^2\right)^{1/2}, \tag{6.15}$$

where $\bar{h}_i$ is the average length of all edges connected to the node corresponding to degree of freedom i. The bilinear weighted interpolant $\pi_H : V \to V_H$ is defined according to

$$\pi_H v = \sum_{i \in \mathcal{M}} \left(\lambda_i^T v\right) \lambda_i. \tag{6.16}$$

The following relation is assumed to hold for $v \in V$:

$$\|v - \pi_H v\|_h \leq CH\|v\| \tag{6.17}$$

where H is the mesh size of the coarse grid and C is a constant. By introducing the modified displacement problem

$$\text{Find } \hat{u} \in V : \qquad v^T K \hat{u} = v^T \pi_H F, \qquad \forall v \in V, \tag{6.18}$$

the assumption (6.17) can be used to derive estimates of the form

$$\|u - \hat{u}\| \leq C\|\bar{F} - \pi_H \bar{F}\|_h \leq CH\|\bar{F}\|, \tag{6.19}$$

where $\bar{F}$ denotes the vector with components $\bar{F}_i = F_i \bar{h}_i^{-2}$. The scaled load vector $\bar{F}$ is $\mathcal{O}(1)$ for a surface distributed load. Based on this, the following proposition regarding the error of the multiscale solution can be formulated.

Proposition 3. *If $\|F - \pi_H F\|_h \leq CH\|F\|$, then*

$$\|u - u_{\text{ms}}\| \leq CH\|\bar{F}\|. \tag{6.20}$$

Next, the error of the localized multiscale solution is investigated. An additional assumption is needed, which states that

$$\max_{w \in V_{\text{ms}}} \min_{v \in \bar{V}_{\text{ms}}} \frac{\|w - v\|}{\|w\|} \leq Ce^{-c\rho}, \tag{6.21}$$

where C and c are constants independent of H. Such relations have been shown to hold for the localized orthogonal decomposition method in its original setup

[46], but remains to be proven for the proposed method in this work. However, with the given assumption the main error bound theorem can be formulated.

Theorem 2. *Assuming equation* (6.21)*, the following error bound is true for any load vector* $F \in V$*:*

$$\|u - \tilde{u}_{\mathrm{ms}}\| \leq C\|\bar{F} - \pi_H \bar{F}\|_h + Ce^{-c\rho}\|\bar{F}\|_h.$$

Finally, some numerical results are presented. A regular square network with $128{\times}128$ nodes are considered. The network is described by the model presented in Chapter 5, and two types of problems are investigated. For the first problem, the boundary of the network is held fixed and a constant diagonal force is applied over the whole network. For the second problem, the left boundary is held fixed while the right boundary is prescribed a non-zero displacement. For the two problem types, three square networks are analysed: one base case, one case with random coefficients in the network model, and one case where the network nodes are perturbed similarly as in Figure 6.1a. See Paper V for a detailed presentation of the simulation setup and results.

In Figure 6.3, the relative energy- and l^2-error are plotted for the first problem type and a network with non-perturbed nodes and a network with random coefficients. The error is compared to the case where the multiscale problem (6.12) is solved with the coarse space V_H, corresponding to classic FEM. It is seen that the two errors are similar for the non-perturbed network while the multiscale method performs much better for a network with randomly varying coefficients. In Figure 6.4, the errors are plotted for the second problem type.

(a) K-error basic.

(b) K-error random coefficients.

(c) l^2-error basic.

(d) l^2-error random coefficients.
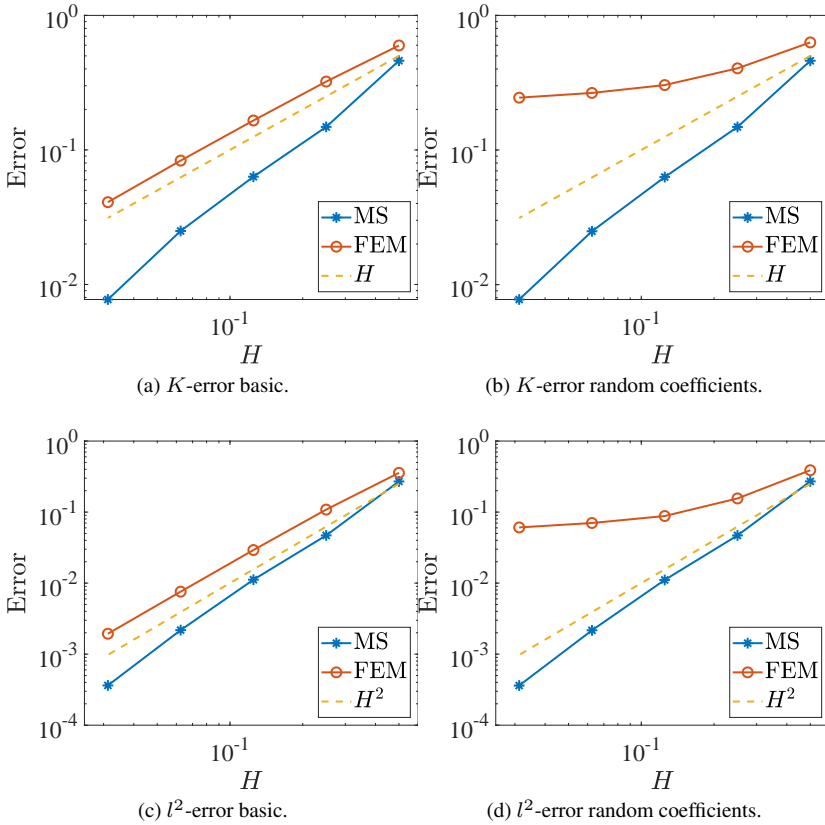
Figure 6.3: Errors for the problem with fixed boundary and constant applied force. The coarse mesh size H and its square H^2 are included in the plots to clarify convergence rates. The so-called FEM-error is included, corresponding to the case where the coarse space V_H is used as solution space.

(a) K-error basic.

(b) K-error random coefficients.

(c) l^2-error basic.

(d) l^2-error random coefficients.

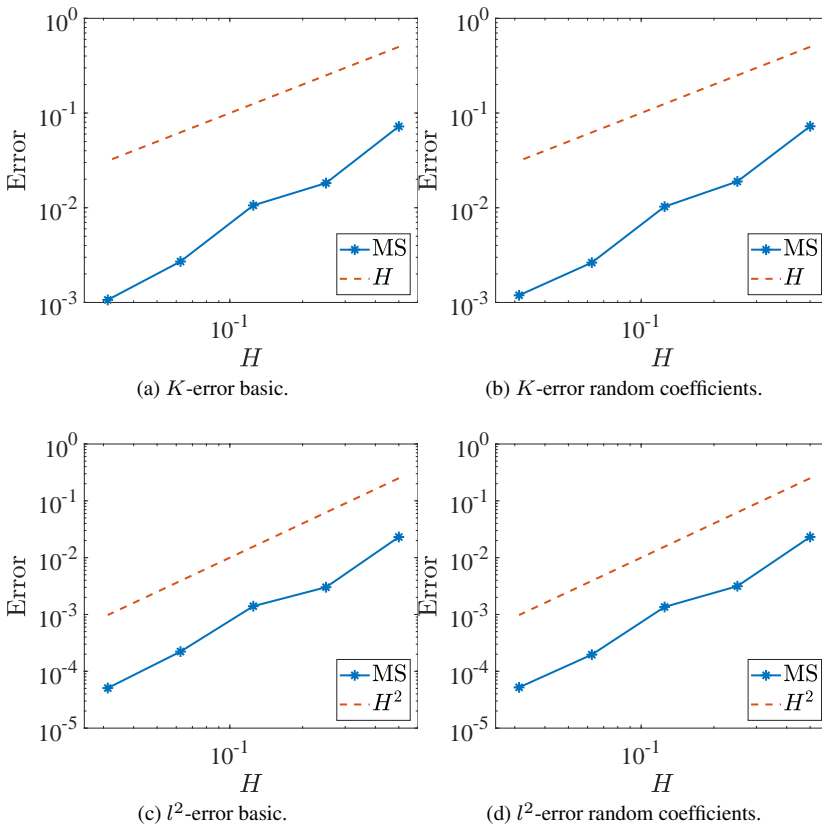Figure 6.4: Errors for the problem with left boundary fixed and right boundary with prescribed non-zero displacement. The coarse mesh size H and its square H^2 are included in the plots to clarify convergence rates.

7. Conclusions and Future Work

Paper making is a complex process through which trees are transformed into a wide range of useful products. Studies of this process are necessary to achieve product and production development, desirable for a worldwide industry. In this work, methods for computer simulation of two parts of the paper making process are developed. On one hand for the paper formation process taking place in the wet end of the paper machine, where the basic structure of paper is formed, and on the other hand for the mechanical properties of the final paper sheets. Accurate and efficient simulation frameworks for these two areas will facilitate comprehensive investigations of how the paper formation influences the properties of the end product.

For the paper formation, a novel fiber-fiber interaction model is developed and incorporated into a framework for simulation of fiber lay downs, including the fluid effect governed by the structure of industrial forming fabrics. Fiber lay downs are simulated and virtual paper sheets are attained. Moreover, the flow over forming fabrics is studied. To enable simulations of the mechanical properties of the resulting sheets, a fiber network model is developed and a numerical multiscale method for fiber networks is proposed, making it possible to simulate large scale sheets while still including each fiber and the bonds in-between.

In this final chapter, the main conclusions of the work are described, and a discussion of possible future work is outlined.

7.1   Conclusions

In this work, numerical methods and simulation tools for paper making are developed. Two main topics are considered, the formation of the paper and the mechanical properties of the resulting sheets.

A new method for calculation of the interaction between fibers is developed. The method includes small scale interaction forces and is based on the DLVO theory. Using a multiscale approach in time makes it possible to resolve interaction forces acting on scales much smaller than the size and motion of the fibers. The interaction model includes a repulsion force giving stability and robustness, necessary for simulation setups with discrete time stepping, that often results in partial overlaps of objects.

A fiber suspension model is presented, in which the novel interaction method is one of four sub-models. The suspension model is incorporated into a framework for simulation of fiber motion in a fluid. The presented framework is robust and powerful, enabling simulations of thousands of fibers whose motion is governed by the fluid flow and the complex interaction between the fibers. The detailed simulation tool can be used to study each single fiber and its motion in the fluid.

The framework is evaluated through lay down simulations, resembling paper forming, with fibers flowing down onto an industrial forming fabric, demonstrating the applicability to create three-dimensional fiber networks which can be used for further investigation of mechanical or penetration properties. The resulting virtual sheets are analysed by simulating the air flow through the sheets before and after pressing. The results show that the fiber geometry affects the permeability of the sheets with reduced air flow through sheets with rectangular fibers cross section compared to circular. Moreover, pressed fiber networks have lower permeability compared to unpressed sheets. The permeability of the simulated sheets agree well with experiments for lower densities, demonstrating the accuracy of the framework. For higher densities, the simulated sheets have higher permeability compared to experiments. This is explained by the one-way coupling simplification removing the effect of self-healing necessary to accumulate small fibers in the fiber network.

The presented simulation framework can also be used to investigate the flow characteristics during the forming process, how different fabric geometries affect the lay down of fibers, and the resulting network configuration.

Studies of the upstream flow over rows of cylinders and three different industrial fabrics illuminate important flow features during the initial part of the formation process. It is shown that for rows of cylinders with uniform cylin-

der diameter and surface spacings similar to real fabric structures, the upstream range of impact of the flow is very short, about one cylinder diameter, and the downstream rows have negligible impact on the upstream features for small surface spacings in the first row. Moreover, it is shown that the transition from steady to un-steady flow, occurring around $Re = 40$, does not change the upstream features. Novel measures are proposed that can be used to characterize the upstream impact of the flow for different cylinder configurations and fabric structures.

The fabric flow investigation shows that it is possible to resolve the flow over industrial forming fabrics in detail. It is shown that the diameter of the wire threads and the displacements between threads give flow impact similar to what is seen in the cylinder study. Moreover, it is concluded that studies of structures with threads with different diameters are necessary to understand additional aspects of the fabric flow. The study shows that the wavelength of the flow periodicity is an important design parameter for fabrics and that large wavelength may increase the risk of drainage marking, based on the features of the simulated flow fields. It is shown that the second layer of a fabric affects the upstream flow if the diameters of its threads are different than the first layer threads. Altogether, detailed flow simulations give important information which can be used when designing fabrics and to understand the impact of the fabric structure on the resulting paper sheet.

To enable simulation of the mechanical properties of largescale paper sheets, described by detailed fiber network models including each fiber and the bonds in-between, a novel upscaling method is developed. First, a fiber network model is proposed based on input from the forming simulations, and used as a basis for the development of the numerical upscaling method. The network model is a mass-spring model and includes a novel force contribution resembling the Poisson effect.

The proposed numerical upscaling method is developed to resolve the mechanics of heterogeneous network models, handling large unstructured systems with highly varying data. The method uses a coarse scale grid to cover the network. Bilinear shape functions defined over the coarse grid give a low-dimensional solution space which is modified by solving sublocal network problems, resulting in corrections of the basis functions. The resulting modified low-dimensional solution space has great approximation properties and the method reduces the maximum size of the problems that have to be solved using localization. The method is proven to give optimal order convergence rates for unstructured and random networks which is not the case for ordinary FEM.

7.2   Future work

The numerical methods and algorithms developed in this work constitute a solid foundation for investigation of paper making by the means of detailed simulations. However, due to the complexity of the paper making process, and the many different parts of the paper production line, there are features that can be added, or parts that can be extended, to the work of this thesis.

The novel fiber-fiber interaction method is mainly evaluated through extensive lay down simulations, demonstrating its good computational performance. However, a more profound numerical and theoretical analysis of the method and the different simplifications employed in this work has to be carried out in the future. For example, different simple test cases with only a few contact points or a few fibers can be investigated by variation of the different parameters, as well as comparing different simplifications of the governing equations for the motion of the contact points.

An important next step of the lay down simulations is to include two-way coupling between fiber and fluid. This is a computational challenging task and it may not be necessary to use full two-way coupling. This should be investigated by comparing the current setup with various semi-coupling approaches. For example a small amount of fibers can be laid down and by freezing the fibers, the flow field can be updated and a new amount of fibers can be laid down, repeating this procedure. Another approach is to resolve the fluid flow more seldom than what is the case for the fibers, by calculating the force on the flow from the fibers and smoothing it out during the longer fluid time steps. By introducing improved two-way coupling, the adhesive feature of the interaction model will probably have a greater impact, and the self-healing phenomena will be included, increasing the retention of fibers. This can be investigated by a simple test case where one fiber is held static and another fiber flows down onto the static fiber comparing two different cases, one with a uniform flow and one where the flow is resolved around the static fiber.

Other parts of the fiber suspension model that can be extended is a more advanced beam model to improve how the fibers conform to the surfaces of each other when laying down. Additional contact and adhesion phenomena in the interaction model, such as friction or hydrogen bonds, may also be investigated.

The simple method for pressing the sheets that currently is employed, where a rigid plate moving at constant speed compresses the fibers, is one feature of the simulation framework that should be improved. In the future, the interaction from the sheet onto the plate should be considered as well as more advanced structures, for example a pressing fabric. Another extension of the lay down

simulation is to consider a non-static fabric and to study different impact angles of the fiber injection.

For the investigation of the upstream flow over cylinders and fabric, which is important during the initial formation, some questions remain to be studied. One important topic is the effect of threads with different diameter, particularly to understand how the second layer threads affect the upstream flow. In the current study it is shown that for structures with the same diameter for all threads, the second layer has negligible upstream impact for the most relevant configurations. However, when investigating the flow through the industrial fabrics, which have different diameters in the different layers, it is shown that the second layer has an impact. This has to be further investigated in the future. Moreover, a second layer positioned in close to contact with the first layer is also of interest to study. Moreover, a measure related to the wavelength of the flow field would be very useful for fabric design.

The fiber network model presented in this work is relatively simple in its nature and is used to test the numerical multiscale method. The model has not yet been used to simulate the mechanical properties of paper sheets. This has to be done in the future to evaluate the simple model by comparing the results with experiments. If the simulation results do not agree with experiments the model has to be extended in a suitable manner. Later on, it should be extended to three dimensions and include large deformations to be able to cover more advanced mechanical simulations. Other features that may be interesting to include is contact between objects and non-linear effects such as plasticity.

The numerical upscaling method proposed in this work has optimal convergence rate for unstructured and random networks. This is shown through numerical examples. Some general error analysis is performed but should be extended in future work by considering a general elasticity matrix and investigate what properties it has to fulfil to guarantee the different error results. Further, the specific matrix given from the network model should be analysed and compared to the requirements given by the error analysis. Additionally, the computational properties of the numerical upscaling method should be investigated, both with respect to time and how large problems that can be solved while retaining acceptable accuracy of the solution. Moreover, fracture propagation problems could be considered using the proposed method.

8. Summary of Papers

Paper I - Novel contact forces for immersed boundary paper forming simulations

Authors: G. Kettil, A. Mark, F. Svelander, R. Lai, L. Martinsson, K. Wester, M. Fredlund, M. Rentzhog, U. Nyman, J. Tryding, and F. Edelvik.

This conference proceeding is from the hundred years anniversary TAPPI conference held in Atlanta, USA, in April 2015. It describes an early version of the object-object interaction model, together with the simulation framework for lay down simulations. Simulation results for lay downs with fibers with circular fiber cross section are included.

Paper II - Detailed simulations of early paper forming

Authors: G. Kettil, A. Mark, F. Svelander, R. Lai, K. Wester, M. Fredlund, M. Rentzhog, and F. Edelvik.

This conference proceeding is from the final COST Action FP1005 conference held in Trondheim, Norway, in June 2015. It is a concise review of the simulation framework at a stage where novel implementations of rectangular fiber cross section and pressing had been accomplished.

Paper III - A multiscale methodology for simulation of mechanical properties of paper

Authors: G. Kettil, A. Målqivst, A. Mark, F. Edelvik, M. Fredlund, and K. Wester.

This conference proceeding is from the 6th European Conference on Computational Mechanics, Glasgow, UK, June 2018. It presents a multiscale framework for simulation of mechanical properties of paper. The forming framework is briefly described. The main focus is on the framework for simulation of the mechanical properties of paper, presenting an overview of the fiber network model and the numerical upscaling method.

Paper IV - Numerical investigation of upstream cylinder flow and characterization of forming fabrics

Authors: G. Kettil, A. Mark, K. Wester, M. Fredlund, and F. Edelvik.

In this paper, the fundamentals of upstream flow over fabrics are studied numerically. First, two-dimensional flow over different configurations of cylinders is investigated. Second, the flow over three industrial forming fabrics is simulated. The resulting flow fields are studied by analysing the upstream flow impact from the structures. Novel measures of the flow impact are defined.

Paper V - Numerical upscaling of discrete network models

Authors: G. Kettil, A. Målqvist, A. Mark, M. Fredlund, K. Wester, and F. Edelvik.

In this paper, the numerical upscaling method for discrete fiber networks is described in detail. The theory of the method is presented and general error analysis is performed. The exponential decay of the corrector functions and the optimal order convergence rate of the method are shown by numerical examples, governed by the fiber network model.

Paper VI - Simulation of paper forming using immersed boundary techniques and a novel fiber interaction method

Authors: G. Kettil, A. Mark, A. Målqivst, F. Svelander, K. Wester, M. Fredlund, and F. Edelvik.

In this paper, the newest version of the interaction model is described. The full framework for lay down simulations is presented, including pressing and cyclic boundary condition for the object interactions. Numerous lay down simulations are performed and the resulting virtual sheets are investigated by simulation of the air flow through the sheets.

Bibliography

[1] Z. (Ed.) Adamzcyk, *Particles at interfaces*, Interface Science and Technology 9, pp. 15-196, 2006.

[2] P. Bajpai, *Biotechnology for Pulp and Paper Processing*, Springer, Boston, pp. 1-4, 2012.

[3] L. A. A. Beex, R. H. J. Peerlings, and M. G. D. Geers, *A multiscale quasicontinuum method for dissipative lattice models and discrete networks*, Journal of the Mechanics and Physics of Solids 64, pp. 154-169, 2014.

[4] G. M. Bell, S. Levine and L. N. McCarthy, *Approximate methods of determining the double-layer free energy of interaction between two charged colloidal spheres*, Journal of Colloid and Interface Science 33 (3), pp. 335-359, 1970.

[5] G. Bossis and J. F. Brady, *Dynamic simulation of sheared suspensions. I. General method*, Journal of Chemical Physics 80 (10), pp. 5141-5154, 1984.

[6] J. F. Brady and G. Bossis, *The rheology of concentrated suspensions of spheres in simple shear flow by numerical simulation*, Journal of Fluid Mechanics 155, pp. 105-129, 1985.

[7] H. Brenner and M. E. O'Neill, *On the Stokes resistance of multiparticle systems in a linear shear field*, Chemical Engineering Science 27 (7), pp. 1421-1439, 1972.

[8] J. Chu, B. Engquist, M. Prodanović, and R. Tsai, *A multiscale method coupling network and continuum models in porous media I: steady-state single phase flow*, Multiscale Modeling & Simulation 10 (2), pp. 515-549, 2012.

[9] F. Della Rossa, C. D'Angelo, and F. Quarteroni, *A distributed model of traffic flows on extended regions*, Networks and Heterogeneous Media 5 (3), pp. 525-544, 2010.

[10] B. V. Derjaguin and L. D. Landau, *Theory of the Stability of Strongly Charged Lyophobic Sols and of the Adhesion of Strongly Charged Particles in Solution of Electrolytes*, Acta Physicochimica URSS 14, pp. 633-662, 1941.

[11] J. V. Doormaal and G. Raithby, *Enhancements of the simple method for predicting incompressible fluid flows*, Numerical Heat Transfer 7 (2), pp. 147-163, 1984.

[12] F. Edelvik, A. Mark, N. Karlsson, T. Johnson, and J. S. Carlson, *Math-based algorithms and software for virtual product realization implemented in automotive paint shops*, In: L. Ghezzi, D. Hömberg, and C. Landry (eds), Math for the Digital Factory, Mathematics in Industry 27, pp. 231-251, 2017.

[13] C. Engwer, P. Henning, A. Målqvist and D. Peterseim, *Efficient implementation of the Localized Orthogonal Decomposition method*, Computer Methods in Applied Mechanics and Engineering 350, pp. 123-153, 2019.

[14] R. Ewing, O. Iliev, R. Lazarov, I. Rybak, and J. Willems, *A simplified method for upscaling composite materials with high contrast of the conductivity*, SIAM Journal on Scientific Computing 31 (4), pp. 2568-2586, 2009.

[15] O. L. Forgacs and S. G. Mason, *Particle motions in sheared suspensions IX. Spin and deformation of threadlike particles*, Journal of Colloid Science 14 (5), pp. 457-472, 1959.

[16] O. L. Forgacs and S. G. Mason, *Particle motions in sheared suspensions X. Orbits of flexible threadlike particles*, Journal of Colloid Science 14 (5), pp. 473-491, 1959.

[17] J. M. Gere and B. J. Goodno, *Mechanics of materials*, Cengage Learning, Stamford, pp. 677-769, 2009.

[18] S. I. Green, Z. Wang, T. Waung, and A. Vakil, *Simulation of the flow through woven fabrics*, Computers & Fluids 37 (9), pp. 1148-1156, 2008.

[19] J. Göhl, A. Mark, S. Sasic, and F. Edelvik, *An immersed boundary based dynamic contact angle framework for handling complex surfaces of mixed wttabilities*, International Journal of Multiphase Flow 109, pp. 164-177, 2018.

[20] J. Göhl, K. Markstedt, A. Mark, K. M. O. Håkansson, P. Gatenholm, and F. Edelvik, *Simulations of 3D bioprinting: Predicting bioprintability of nanofibrillar inks*, Biofabrication 10 (3), 034105, 2018.

[21] H.C. Hamaker, *The London-van der Waals Attraction Between Spherical Particles*, Physica 4 (10), pp. 1058-1072, 1937.

[22] J. Happel and H. Brenner, *Low Reynolds Number Hydrodynamics*, Prentice-Hall, Englewood Cliffs, New Jersey, 1965.

[23] F. Hellman and A. Målqvist, *Contrast independent localization of multiscale problems*, Multiscale Modeling & Simulation 15 (4), pp. 1325-1355, 2017.

[24] P. Henning and A. Målqvist, *Localized orthogonal decomposition techniques for boundary value problems*, SIAM Journal on Scientific Computing 36 (4), pp. A1609-A1634, 2014.

[25] A. C. Hindmarsh, P. N. Brown, K. E. Grant, S. L. Lee, R. Serban, D. E. Shumaker, and C. S. Woodward, *SUNDIALS: Suite of Nonlinear and Differential/Algebraic Equation Solvers*. ACM Transactions on Mathematical Software, 31 (3), pp. 363-396, 2005.

[26] G. J. Hirasaki and J. D. Hellums, *A general formulation of the boundary conditions on the vector potential in three-dimensional hydrodynamics*, Quarterly of Applied Mathematics 26 (3), pp. 331-342, 1968.

[27] U. Hirn, and R. Schennach, *Comprehensive analysis of individual pulp fiber bonds quantifies the mechanisms of fiber bonding in paper*, Scientific Reports 5, id. 10503, 2015.

[28] T. J. R Hughes, G. R. Feijóo, L. Mazzei, and J. B. Quincy, *The variational multiscale method - a paradigm for computational mechanics*, Computer Methods in Applied Mechanics and Engineering 166 (1-2), pp. 3-24, 1998.

[29] T. Y. Hou, X. Wu, *A multiscale finite element method for elliptic problems in composite materials and porous media*, Journal of Computational Physics 134 (1), pp. 169-189, 1997.

[30] A. Ibrahimbegović and M. A. Mikdad, *Finite rotations in dynamics of beams and implicit time-stepping schemes*, International Journal for Numerical Methods in Engineering 41 (5), pp. 781-814, 1998.

[31] O. Iliev, R. Lazarov, and J. Willems, *Fast numerical upscaling of heat equation for fibrous materials*, Computing and Visualization in Science 13 (6), pp. 275-285, 2010.

[32] S. Ingelsten, A. Mark, and F. Edelvik, *A Lagrangian-Eulerian framework for simulation of transient viscoelastic fluid flow*, Journal of Non-Newtonian Fluid Mechanics 266, pp. 20-32, 2019.

[33] J. N. Israelachvili, Intermolecular and Surface Forces: Revised Third Edition, Academic Press (2011).

[34] G. B. Jeffery, *The Motion of Ellipsoidal Particles Immersed in a Viscous Fluid*, Proceedings of the Royal Society of London A 102 (715), pp. 161-179, 1922.

[35] T. Johnson, A. Mark, J. Nyström, S. Rief, M. Fredlund, M. Rentzhog, U. Nyman, J. Tryding, R. Lai, L. Martinsson, K. Wester, and F. Edelvik, *A multi-scale simulation method for the prediction of edge wicking in multi-ply paperboard*, Nordic Pulp and Paper Research Journal 30 (4), pp. 640-650, 2015.

[36] P. Kortelainen, R. Kilpeläinen, S. Taipale, A. Marin, S. Metsäranta, S. Lohm, and E. Sjöblom, *Forming fabrics*, In: Paulapuro, H. (ed.): Papermaking Part 1, Stock Preparation and Wet End, Paperi ja Puu Oy, Helsinki, pp. 310-340, 2008.

[37] S. B. Lindström and T. Uesaka, *Simulation of the motion of flexible fibers in viscous fluid flow*, Physics of Fluids 19 (11), 113307, 2007.

[38] S. B. Lindström and T. Uesaka, *Simulation of semidilute suspensions of non-Brownian fibers in shear flow*, Journal of Chemical Physics 128 (2), 024901, 2009.

[39] A. Mark, B. Andersson, S. Tafuri, K. Engström, H. Söröd, F. Edelvik, and J. S. Carlson, *Simulation of electrostatic rotary bell spray painting in automotive paint shops*, Atomization and Sprays 23 (1), pp. 25-45, 2013.

[40] A. Mark, R. Rundqvist, and F. Edelvik, *Comparison Between Different Immersed Boundary Conditions for Simulation of Complex Fluid Flows*, Fluid Dynamics and Materials Processing 7 (3), pp. 241-258 (2011).

[41] A. Mark, E. Svenning, R. Rundqvist, F. Edelvik, E. Glatt, S. Rief, A Wiegmann, M. Fredlund, R. Lai, L. Martinsson, and U. Nyman, *Microstructure Simulation of Early Paper Forming Using Immersed Boundary Methods*, TAPPI Journal 10 (11), pp. 23-30, 2011.

[42] A. Mark, J. Tryding, J. Amini, F. Edelvik, M. Fredlund, M. Glatt, R. Lai, L. Martinsson, U. Nyman, M. Rentzhog, S. Rief, and A. Wiegmann, *Modeling and Simulation of Paperboard Edge Wicking*, Nordic Pulp and Paper Research Journal 27 (2), pp. 397-402, 2012.

[43] A. Mark, J. Tryding, J. Amini, F. Edelvik, M. Fredlund, M. Glatt, R. Lai, L. Martinsson, U. Nyman, M. Rentzhog, S. Rief, and A. Wiegmann, *Multiscale Simulation of Paperboard Edge Wicking Using A Fiber-resolving Virtual Paper Model*, Tappi Journal 11 (6), pp. 9-14, 2012.

[44] A. Mark and B. G. M. van Wachem, *Derivation and validation of a novel implicit second-order accurate immersed boundary method*, Journal of Computational Physics 227 (13), pp. 6660-6680, 2008.

[45] J. Mohd-Yusof, *Combined immersed-boundary/b-spline methods for simulations of flow in complex geometries*, Technical report, Center for Turbulence Research, Annual Research Briefs, pp. 317-326, 1997.

[46] A. Målqvist and D. Peterseim, *Localization of elliptic multiscale problems*, Mathematics of Computation 83 (290), pp. 2583-2603, 2014.

[47] N. M. Newmark, *A method of computation for structural dynamics*, Journal of Engineering Mechanics (ASCE) 85 (3), pp. 67-94, 1959.

[48] D. Nowak, T. Andersson, T. Johnson, K. Küfer, A. Mark, and F. Edelvik, *Multiobjective optimization of a heat-sink design using the sandwiching algorithm and an immersed boundary conjugate heat transfer solver*, Journal of Heat Transfer 140 (10), 102002, 2018.

[49] M. Ostoja-Starzewski, *Lattice models in micromechanics*, Applied Mechanics Reviews 55 (1), pp. 35-60, 2002.

[50] C. S. Peskin, *Numerical analysis of blood flow in the heart*, Journal of Computational Physics 25 (3), pp. 220-252, 1977.

[51] C. S. Peskin and D. M. McQueen, *Computational biofluid dynamics*, in Fluid Dynamics in Biology: Proceedings of the AMS-IMS-SIAM joint Summer Research Conference on Biofluid Dynamics, Contemporary Mathematics, Vol. 141, edited by A. Y. Cheer and C. P. van Dam (Am. Math. Soc. Providence, RI, 1993), p. 161186.

[52] C. Rhie and W. Chow, *Numerical study of the turbulent flow past an airfoil with trailing edge separation*, AIAA Journal 21 (11), pp. 1527-1532, 1983.

[53] R. F. Ross and D. J. Klingenberg, *Dynamic simulation of flexible fibers composed of linked rigid bodies*, Journal of Chemical Physics 106 (7), pp. 2949-2960, 1997.

[54] L. Schiller and A. Naumann, *Uber die grundlegenden Berechnung bei der Schwerkraftbereitung*, Zeitschrift des Vereins Deutscher Ingenieure 77 (12), pp. 318-320 (1933).

[55] C. F. Schmid, L. H. Switzer, and D. J. Klingenberg, *Simulations of fiber flocculation: Effects of fiber properties and interfiber friction*, Journal of Rheology. 44 (4), pp. 781-809, 2000.

[56] L. Simão, D. Hotza, F. Raupp-Pereira, J. A. Labrincha, and O. R. K. Montedo, *Wastes from pulp and paper mills - a review of generation and recycling alernatives*, Cerâmica 64 (371), pp. 443-453, 2018.

[57] J. C. Simo, *A finite strain beam formulation. The three-dimensional dynamic problem. Part I*, Computer Methods in Applied Mechanics and Engineering 49 (1), pp. 55-70, 1985.

[58] J. C. Simo and L. Vu-Quoc, *A three-dimensional finite-strain rod model. Part II: Computational aspects*, Computer Methods in Applied Mechanics and Engineering 58 (1), pp. 79-116, 1986.

[59] J. C. Simo and L. Vu-Quoc, *On the dynamics in space of rods undergoing large motions - a geometrically exact approach*, Computer Methods in Applied Mechanics and Engineering 66 (2), pp. 125-161, 1988.

[60] J. M. Stockie, *Simulating the dynamics of flexible wood pulp fibres in suspension*, in: Proceedings of the 16th Annual International Symposium on High Performance Computing Systems and Applications, IEEE Computer Society, p. 154-160, 2002.

[61] J. M. Stockie and S. I Green, *Simulating the Motion of Flexible Pulp Fibres Using the Immersed Boundary Method*, Journal of Computational Physics 147 (1), pp. 147-165, 1998.

[62] E. Svenning, A. Mark, F. Edelvik, et al., *Multiphase Simulation of Fiber Suspension Flows Using Immersed Boundary Methods*, Nordic Pulp and Paper Research Journal 27 (2), pp. 184-191, 2012.

[63] L. H. Switzer and D. J. Klingenberg, *Rheology of sheared flexible fiber suspensions via fiber-level simulations*, Journal of Rheology. 47 (3), pp. 759-778, 2003.

[64] L. H. Switzer and D. J. Klingenberg, *Flocculation in simulations of sheared fiber suspensions*, International Journal of Multiphase Flow 30 (1), pp. 67-87, 2004.

[65] E. J. W. Vervey and J. Th. G. Overbeek, *Theory of the Stability of Lyophobic Colloids*, Elsevier, Amsterdam (1948).

[66] E. Weinan, B. Engquist, *The heterogeneous multiscale methods*, Communications Mathematical Sciences 1 (1), pp. 87-132, 2003.

[67] D. V. Wilbrink, L. A. A. Beex, and R. H. J. Peerlings, *A discrete network model for bond failure and frictional sliding in fibrous materials*, International Journal of Solids and Structures 50 (9), pp. 1354-1363, 2013.

[68] S. Yamamoto and T. Matsuoka, *A method for dynamic simulation of rigid and flexible fibers in a flow field*, Journal of Chemical Physics 98 (1), pp. 644-650, 1993.

[69] S. Yamamoto and T. Matsuoka, *Viscosity of dilute suspensions of rodlike particles: A numerical simulation method*, Journal of Chemical Physics 100 (4), pp. 3317-3324, 1994.

[70] S. Yamamoto and T. Matsuoka, *Dynamic simulation of fiber suspensions in shear flow*, Journal of Chemical Physics 102 (5), pp. 2254-2260, 1995.

[71] M. M. Zdravkovich, *Review - review of flow interference between two circular cylinders in various arrangements*, Journal of Fluids Engineering 99 (4), pp. 618-633, 1977.

[72] M. M. Zdravkovich, *Flow around circular cylinders Vol 1: Fundamentals*, Oxford Univesity Press, Oxford, pp. 3-16, 1997.